Material Budget Studies for the Belle II Detector

Waleed Ahmed
Department of Physics
McGill University

July 2017

A thesis submitted to McGill University in partial fulfilment of the requirements of the degree of M.Sc

Abstract

The Belle II experiment at the KEK laboratory in Tsukuba, Japan is currently undergoing commissioning, with first physics data anticipated in 2018. Understanding the material distribution of detector components is of critical importance for precision e^+e^- collider experiments like Belle II, as the density and distribution of this material impacts tracking and vertex reconstruction, as well as other aspects of detector performance. Two complementary approaches undertaken to carry out material studies at Belle II are presented here. The first part involves a comparison of precise 2D images of the material profile of the vertex detectors, obtained using test beam experiments with high resolution tracking telescopes, with the detector model implemented in the Belle II simulation. This new approach represents one of the most precise material studies in the field. The second part of the thesis is a presentation of detailed studies of material profiles of other components of the Belle II detector with a focus on explaining the changes found in the different versions of the detector simulation.

Résumé

La Belle II est une expérience au laboratoire KEK à Tsukuba, le Japon est en cours de mise en service, avec les premires données de physique prévues en 2018. La compréhension de la distribution matérielle des composants du détecteur revêt une importance cruciale pour les essais de précision e^+e^- collider comme Belle II, car la densité et la répartition de ce matériau impactent le suivi et la reconstruction des sommets, ainsi que d'autres aspects de la performance du détecteur. Deux approches complémentaires visant à mener des études de matériaux à Belle II sont présentées ici. La premiére partie implique une comparaison d'images 2D précises du profil matériel des détecteurs de sommet, obtenus à l'aide d'expériences de faisceau de test avec des télescopes de suivi haute résolution, avec le modéle de détecteur mis en œuvre dans la simulation Belle II. Cette nouvelle approche représente une des études de matériaux les plus précises sur le terrain. La deuxiéme partie de la thése est une présentation d'études détailles des profils de matériaux d'autres composants du détecteur Belle II en mettant l'accent sur les modifications apportées aux différentes versions de la simulation du détecteur.

Acknowledgements

I thank my supervisor Dr. Steven Robertson for giving me the opportunity to work on Belle II and being extremely supportive throughout my time at McGill as a master's student. I am particularly grateful for having had the chance to visit the KEK lab to see the experiment and experience Japanese culture. Fellow group members Andrea, Helena and Rob have been an important source of support and have served as collaborators, friends and travel companions. Dr. Andreas Warburton's friendliness and his critical eye has served me well.

I also want to thank my collaborators Benjamin Schwenker and Ulf Stolzenberg for giving me the opportunity to contribute to their unique project on the vertex detectors. I am grateful for their constant support and patience with me as I tried to juggle coursework and research. This thesis would not have been possible without the help of all the detector sub-system specialists who took the time out to share important details about their detectors. I am greatly indebted to all of them and would like to particularly thank: Alexei Sibidanov (ECL), Luka Sentelj (ARICH), Makato Uchida (CDC), Marko Staric (TOP) and Leo Piilonen (KLM). Special thanks to Torben Furber and Alex Beaulieu for their technical support throughout my thesis.

Lastly, I am grateful to my parents, my mother in particular, for their love and support; my brother for holding down the fort for me and my sister for her compassion and kindness.

Preface and Contributions of Authors

All sections of this thesis were written by myself, the main author. Unless stated otherwise, I also generated all the plots for the analysis in chapters 5 and 6.

I also gratefully acknowledge the support and assistance of my collaborators, Benjamin Schwenker and Ulf stolzenberg, whose contributions to publications are described below.

— Ulf Stolzenberg et al. Radiation length imaging using high resolution telescopes. 2016 *Appears in Chapter 5*

Contents

List of Figures

List of Tables

1
Introduction

The Belle II experiment is a high energy particle physics experiment at the SuperKEKB accelerator in Tsukuba, Japan. The detector is an upgrade to the original Belle experiment with the luminosity improved by 40 times; it is expected to start its physics run in 2018. Several upgrades have been made to the detector to adjust to the new high-luminosity environment such as addition of a new pixel vertex detector right at the interaction point. The goal of Belle II is to search for evidence of new physics through a large number of precision measurements that are sensitive to physics beyond the Standard Model. Such measurements include rare and forbidden decays of B-mesons, asymmetries such as CP (Charge Parity) violation in B-meson, charm, and tau decays.

The goal of this thesis was to study the material content in the Belle II detector simulation. Chapter 2 describes the motivation behind these studies and the relevant theory needed. Since the entire detector was studied in this thesis, details of the purpose and design of each subsystem are given in Chapter 3. Chapter 4 explains the two techniques employed to conduct the material studies: use of radiation length imaging and the material scan tool of the Belle II software framework. Material studies on the vertex detectors using radiation length imaging are detailed in Chapter 5. Finally, Chapter 6 describes the overall material studies of the Belle II detector simulation.

2
Theory

It is only through the interaction with everyday matter that subatomic particles can be detected. The objective of this section is thus to summarize the nature of these interactions in order to get a better appreciation of the impact that material can have in a physics measurement. Studying and accurately modeling the material is vital in a particle physics experiment as extra material in the detector can lead to a multitude of issues such as unwanted scattering and electromagnetic showers, the degradation of momentum resolution and the misidentification of interaction vertices. While the interactions between particles and detector material is an extensive topic, the physical processes relevant to this thesis are summarized below. Prior to the discussion on these interactions, a brief summary of the Standard Model is presented which summarizes the fundamental particles and forces of nature.

2.1 The Standard Model (SM)

The SM of particle physics is the most comprehensive theory which describes elementary particles and their interaction with the fundamental forces of nature. The primary physics objective of Belle II is to carry out high-precision measurements that can probe predictions of the SM and observe any deviations for signs of new physics.

The SM is a quantum field theory described by the gauge symmetry group $SU(3)\times SU(2)\times U(1)$. The Lagrangian of the SM describes the internal symmetries and the dynamics of the theory. In this formalism, the elementary particles are described in terms of excitation of dynamical fields, while the forces are represented by gauge fields which act on these dynamical fields [1].

According to the SM, all of matter is made out of three types of elementary particles: leptons, quarks and bosons. The leptons are spin-$1/2$ particles classified according to their charge (Q), electron number (L_e), muon number (L_μ) and tau number (L_τ). These are the electron (e) and electron neutrino (ν_e), muon (μ) and muon neutrino (ν_μ), tau (τ) and tau neutrino (ν_τ); these fall into three $generations$ as shown in figure 2.1. The charged leptons carry a charge of -1 and their corresponding neutrinos have zero charge. Similarly, the quarks are categorized into six $flavours$ which are classified as up (u), down (d), charm (c), strange (s), truth (t) and beauty (b). They carry fractional charges and are also spin-$1/2$ like the leptons. Additionally, the quarks carry a "colour" charge (referred to as red, blue and green) which is an additional conserved quantum number and acts as the equivalent of charge for the strong force; it helps explain why individual quarks don't occur in nature due to the phenomenon of colour confinement. [2]

The bosons are integer spin particles; the gauge bosons mediate the interactions between the particles. The number of generators of a specific symmetry group dicatate the number of gauge fields, therefore there are 8+3+1 gauge bosons, each corresponding to a part of the $SU(3)\times SU(2)\times U(1)$ group. Three of the four fundamental forces and their mediators are summarized below [1–3](since there is no consistent quantum theory of gravity and it doesn't impact particle physics observations, it is not accounted for in the SM and is explained by General

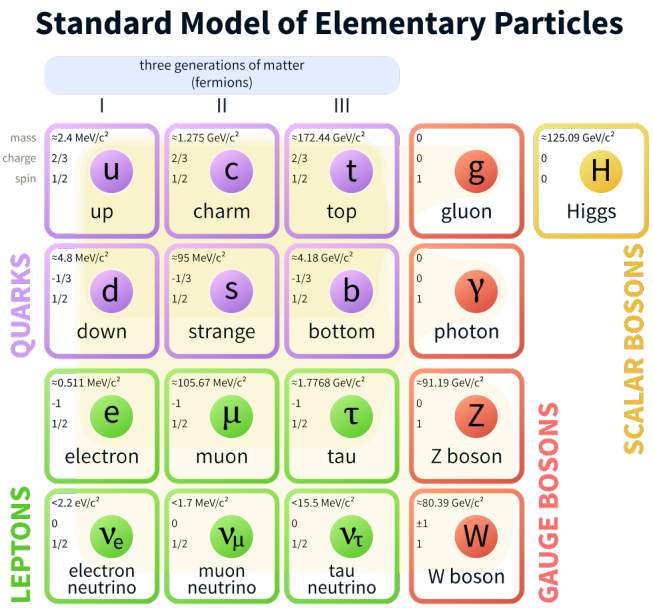

Figure 2.1 – A table summarizing the fundamental particles of the Standard Model [4].

Relativity instead):

• The electromagnetic (EM) force: This force is most common force we encounter in our everyday life. It explains the force between charge carrying particles such as electrons and protons. It is associated with the $U(1)$ gauge group and is mediated by the photon (γ) which is a massless spin-1 particle and carries no charge. Relative to the strong force, its strength is 10^{-2} at the proton scale (i.e. when comparing the force at the range of the distance between two protons).

• The weak force: Unknown in classical physics, this force acts on all fermions since they carry a flavour. It can change quarks from one type to another; it thus accounts for phenomenon such as nuclear beta decay and is quite important for the flavour physics carried out by Belle II. The most important feature of the weak force is that it is chiral i.e. it only couples to left handed fermions (and right handed anti-fermions). Compared to the strong force, it is weaker by 10^{-13} at the

proton scale.

The force is associated with three spin-1 particles of $SU(2)$ gauge group, the $W^{\pm}$ and Z^0 which mediate the force. Unlike the other forces, the mediators for the weak force have mass which explains the relative weakness of the force. At high energies, the weak force and the electromagnetic force are combined into the electroweak force under the $SU(2) \times U(1)$ gauge group [5].

• The strong force: It explains the interaction of particles that carry the colour charge. It accounts for the stability of the atom despite the self-repulsion from positively charged protons in the nucleus. Eight spin-1 massless particles of the $SU(3)$ group called gluons mediate the strong force; any particle that couples to this gauge group is said to carry colour. At the proton scale, the force is 100 times stronger than the EM force.

Hadrons are composite particles made up of quarks. There are two main types of hadrons: mesons, made of two quarks (a quark and anti-quark), and baryons which are made of either three quarks or anti-quarks. Due to the various possible combinations of quarks that can be formed, there are a large number of hadrons that can be created in particle accelerators such as pions (π), kaons (K) and lambda (Λ) particles. In the case of the Belle II, hadrons called B-mesons, which contain a b quark or antiquark, are probably one of the most important. Precision studies of the decay of B-mesons can shed important insight into phenomenon such as CP-violation and point to hints for new physics [2].

2.2 Interactions of Charged Particles with Matter

Subatomic particles can interact with material through either the electromagnetic, weak or strong force. Electromagnetic interactions that involve the excitation and ionization of electrons in the absorbing material are the most common. In the case of relativistic particles, mechanisms such as Bremsstrahlung and Cherenkov radiation are important as well. Energy loss of an incident particle as a result of these processes is elaborated in more details below.

2.2.1 Energy loss due to ionization and excitation

At non-relativistic energies, the primary method of energy loss for charged particles is through electromagnetic interactions between the moving particle and the detecting material. Since the electromagnetic interaction is long range, a direct collision isn't necessary for energy transfer; it can be accomplished by passing close to the atomic nuclei of the absorbing material. As a particle traverses a material, it can either excite the atoms of the absorbing material and raise its electrons to a higher energy level (excitation) or it can completely remove them from the atom (ionization) [6].

The average energy loss (or "stopping power") dE per length dx is given by the Bethe-Bloch formula in units of MeV/(g/cm^2) by [7],

$$\left\langle \frac{dE}{dx} \right\rangle = \frac{4\pi}{m_e c^2} \cdot \frac{nz^2}{\beta^2} \cdot \left(\frac{e^2}{4\pi\varepsilon_0} \right)^2 \cdot \left[\ln\left(\frac{2m_e c^2 \beta^2}{I \cdot (1-\beta^2)} \right) - \beta^2 \right], \tag{2.1}$$

where c is the speed of light, ϵ_0 the vacuum permittivity, I is the mean excitation energy of the material, $\beta = \frac{v}{c}$ with v being the velocity of the particle, z is the charge

of the incident particle, n is the electron number density, e and m_e the electron charge and rest mass respectively. The electron density of the material is given by, $n = \frac{N_A \cdot Z \cdot \rho}{A \cdot M_u}$ where ρ is the density of the material, Z is the atomic number of the absorber and A is its relative atomic mass, N_A the Avogadro number and M_u is the molar mass constant.

The role of the absorbing material is evident from this expression as the energy loss is directly proportion to Z. It can also be seen that the mass of the incident particle doesn't play a role; its velocity and charge are the main parameters.

2.2.2 Bremsstrahlung and Radiation Length

Bremsstrahlung comes from a German word which translates literally to "braking radiation". It occurs when charged particles lose their energy due to interactions with the Coloumb field of the nuclei of the absorbing material. As the charged particle is decelerated in this Coulomb field, a fraction of its energy is emitted in the form of photons. The energy loss by bremsstrahlung is given by [8],

$$-\frac{dE}{dx} = 4\alpha \left(\frac{1}{4\pi\varepsilon_0}\frac{e^2}{Mc^2}\right)^2 \left(\frac{N_A Z^2}{A}\right) z^2 E \ln\left(\frac{183}{Z^{1/3}}\right), \tag{2.2}$$

where $\alpha = 1/137$ is the fine structure constant and the remainder of the variables hold the same meaning as the Bethe-Bloche formula above. As this equation shows, unlike in the case of ionization, the energy loss is proportional to the energy of the incident particle and square of the atomic number of the absorbing material, while it is inversely proportional to the incident particles mass squared. Thus, for high energy electrons and positrons this process becomes the predominant way in which they loose their energy in a given material; whereas for muons,

bremsstrahlung is relatively small for energy scales of relevance to experiments like Belle II.

The energy loss equation by bremsstrahlung for electrons and positrons can be re-written in terms of a new parameter which is defined as the radiation length X_0. The equation above then becomes [8],

$$-\frac{dE}{dx} = \frac{E}{X_0}, \tag{2.3}$$

where

$$X_0 = \frac{1}{4\alpha}\left(4\pi\varepsilon_0\frac{m_e c^2}{e^2}\right)^2\left(\frac{A}{N_A Z^2}\right)\frac{1}{\ln\left(\frac{183}{Z^{1/3}}\right)}. \tag{2.4}$$

The radiation length X_0 is then interpreted as (a) the mean distance over which a high-energy electron loses all but $1/e$ of its energy by bremsstrahlung, and (b) $7/9$ of the mean free path for pair production by a high-energy photon [7] (pair-production is described in the following section). X_0 is a characteristic of the material and is used as a measure of its thickness in terms of the ability of electromagnetic particles to penetrate it; it is also the appropriate scale length for describing high-energy electromagnetic cascades. X_0 is expressed in units of g/cm^2; it can also be given in units of cm by multiplying it by the density of the material. More often, it is expressed by the ratio X/X_0 which is a dimensionless quantity and gives a measure of the thickness of the material in units of radiation lengths.

2.2.3 Pair Production

At high energies, other energy loss mechanisms come into play in addition to Bremsstrahlung. In pair production, a high energy photon converts into

an electron-positron pair. This process can't happen in free space and requires interaction with the Coloumb field of another nuclei in order to conserve energy and momentum. The rest energy of an electron is 0.51 MeV; thus this process is energetically not possible for photons of energies less than 1.02 MeV [6].

Electromagnetic cascades, or showers, can occur when a high energy photon released by bremsstrahlung creates an electron positron pair via pair production. These two particles create another photon again through bremsstrahlung and the process continues to create a shower with increasing number of particles. This cascade can penetrate deep into the material and continues until the photon energies drop below the threshold for pair production and the cascade of electrons and positrons "range out" in the medium via ionization [6].

2.2.4 Multiple Coulomb scattering

As a charged particle traverses a medium, it is scattered by the Coulomb potentials of its nuclei and electrons. Unlike in the case of ionization and excitation, the energy loss isn't due to the collisions with atomic electrons but is due to interactions with the Coulomb field in the nuclei. The distribution of scattering angles due to Coulomb scattering is described by Moliere's theory [8]. For small scattering angles, the distribution is Gaussian around the average scattering angle $\theta = 0$; there are also less frequent "hard-scatters" caused by collisions with nuclei which produce non-Gaussian tails. The root mean square of the projected scattering-angle distribution is given by [7],

$$\theta_{rms} = \frac{13.6\text{MeV}}{\beta cp}\sqrt{\frac{x}{X_0}}z[1 + 0.038\ln(x/X_0)], \tag{2.5}$$

where p is the momentum, βc is the velocity, z is charge of the scattered particle. x/X_0 is the thickness of the scattering medium, expressed in units of radiation length as explained earlier. This equation is particularly important for material studies since it relates scattering angles to the radiation length of the material. As will be seen in Chapter 4, multiple Coulomb scattering plays a vital role when it comes to determining the amount of material in the vertex detector for this experiment. It is also the reason why material studies are important since scattering degrades the tracking performance of the detector.

To get an idea of the impact extra material can cause on the physics measurement, the equation above can be used to estimate of the impact on the reconstruction of tracks. Since the scattering angle is proportional to $\sqrt{\frac{x}{X_0}}$, based on one study, a change of 1 % of X_0 results in a scattering angle of θ_{rms} = 0.25° for an electron with with a momentum of 1 GeV/c; for a 300 MeV/c pion the scattering angle is 1° [9]. Low momentum also impacts the scattering angle as both β and p are inverselely proportional to it. According to another study, 50 MeV/c pions have a standard deviation of scattering angles from their original trajectory by more than 2 degrees when passing a single layer of the Belle II Silicon Vertex Detector (SVD). Whereas, for 1 GeV pions, this value is only 0.04 degrees i.e. 50 times smaller [10].

2.2.5 Cherenkov Radiation

When a charged particle with velocity v traverses a material of an index of refraction n and its velocity exceeds the speed of light c/n in that material, then it emits electromagnetic radiation called Cherenkov radiation [8]. This occurs because the charged particle polarizes the atoms along its path which results in the creation of electric dipoles. The time variation of the dipole fields leads to the

creation of electromagnetic radiation. For $v < c/n$, the dipoles are symmetrically arranged around the particle track so the net dipole field vanishes. However, for $v < c/n$, this symmetry is broken and results in a non-zero net dipole moment which creates radiation [8].

The angle between the emitted Cherenkov photons and the particle track is given by,

$$\cos\theta_c = \frac{1}{\beta n}, \tag{2.6}$$

where n is the refractive index, and β is v/c where v is the particles velocity and c is the speed of light. For a fixed energy, the Lorentz factor depends on the mass of the particle. Thus, measurement of Cherenkov radiation is a useful technique for particle identification purposes as is elaborated on further in Chapter 3.

3

The Belle II Experiment

This chapter covers an overview of the SuperKEKB particle accelerator and the Belle II detector. Unless stated, all information is extracted from Technical Design Report referenced in [11].

3.1 The SuperKEKB Accelerator

The SuperKEKB is the successor to the KEKB particle accelerator used for the original Belle experiment and operated from 1998 to 2010 by KEK, the Japanese High-Energy Accelerator Research Organization. The SuperKEKB has a circumference of 3km and is located 10m below the ground; the general setup can be seen in figure 3.1. It is an asymmetric e^+ e^- collider designed to operate at a center-of-mass energy of$\sqrt{s} = 10.58$ GeV with the e^+ and e^- beams operating at 7 GeV and 3.5 GeV respectively. The center-of-mass energy is chosen such that it corresponds to the $\Upsilon(4S)$-resonance. This resonance is important because it allows for a decay into a pair of B mesons with a branching ratio of 96%; about half of them decaying to B^+B^- and the other half to $B^0\overline{B}^0$, thus effectively creating a "B-factory" [12]. In addition, the mass of the $\Upsilon(4S)$-resonance is nearly the same as that of the B meson pairs and thus the mesons are created nearly at rest in the center-of-mass frame.

The asymmetry in the beam energies boosts the newly created B meson pairs in the direction of the higher energy beam in the lab frame; the Lorentz boost factor is $\beta\gamma = 0.425$ [13]. This allows for measurements of time dependent CP-violation through the relative decay lengths of the B mesons; one of the main objectives of the experiment. Unlike hadron colliders, electron-positron collisions result in complete annihilation with the initial conditions well-known; the only background is from beam interactions and this results in a much cleaner environment for precision studies.

The upgrades to the SuperKEKB will result in an instantaneous luminosity of 8 $\times 10^{35}$ cm^{-2}s^{-1} which is 40 times that of the previous Belle experiment. Over the course of its life, the experiment will accumulate over 50 ab^{-1} of integrated luminosity as shown in figure 3.2. Reaching higher luminosities requires increasing the beam current or reducing the beam size at the interaction point (IP). The SuperKEKB relies on both methods to accomplish this, having doubled the beam current and squeezing the beams to the nano-meter scale.

These changes to the beam parameters also greatly increases the background rates due to self-interaction of the beams and due to interaction with residual gas in the beam pipes [14]. Since the main background source, the Touchek Effect, is proportional to E^{-3}, the asymmetrical beam energies were set to the aforementioned values to mitigate this effect.

The first beams of the SuperKEKB came online in February 2016 with a commissioning detector called BEAST-II. This will be followed by a second run in 2017 without the vertexing detectors installed to test if the radiation levels are safe for them. Finally, the physics run with a fully operational Belle II detector and SuperKEKB is scheduled to start in late 2018 [14].

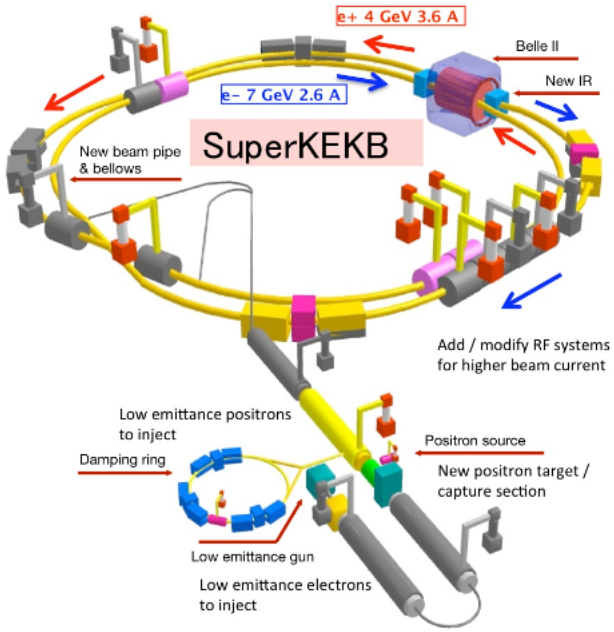

Figure 3.1 – Schematic of the SuperKEKB Accelerator [13].

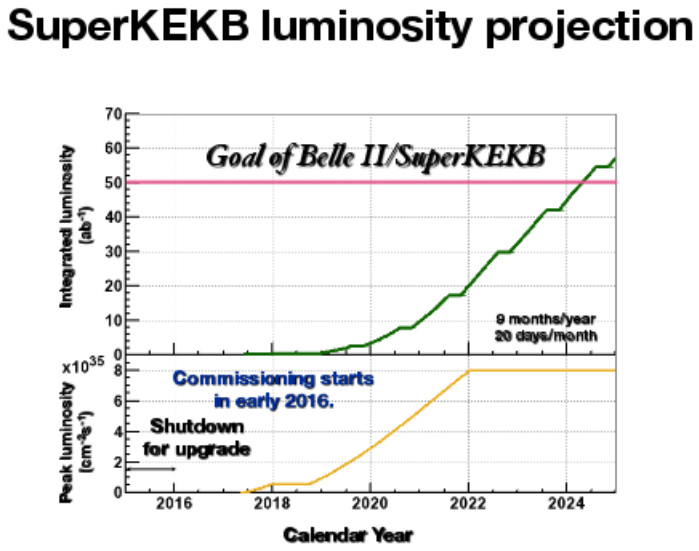

Figure 3.2 – Projected data taking for Belle II over the period of its commissioning and operation. The green curve indicates the integrated luminosity while the yellow is the peak luminosity for the experiment [12].

3.2 The Belle II Detector

The Belle II detector is a general purpose spectrometer designed to study the decay of $B\bar{B}$ pairs created via e^+e^- collisions by the SuperKEKB particle accelerator. It has a cylindrical geometry and is configured around a superconducting solenoid coil which produces a magnetic field of 1.5 T. Due to the boost created by the asymmetry of the beams, there is greater coverage in the front end i.e. the direction in which the centre- of-mass system is boosted relative to the lab frame. The detector was designed to provide good vertex and momentum resolution, along with efficient identification of e, K, and π to facilitate B-flavour tagging [15].

The detector aims at full reconstruction of all particles and provides an acceptance, in the lab frame, of θ = 17° to 180° in the polar angle and ϕ = 0° to 360° in the azimuth angle. The coordinate system defined in Belle II is a right handed system using the x,y and z as the axis and the interaction point (IP) as the origin. The z-axis is parallel to the beam with the y-axis pointing upwards. The radial distance from the interaction point, $r = \sqrt{x^2 + y^2}$, is the distance projected on the the xy plane. θ subtends between the z and y axis while the ϕ extends about the z-axis. A schematic outlining the general detector and its primary subsystem is shown in figure 3.3. [13].

3.2.1 Pixel Vertex Detector (PXD)

The primary purpose of the PXD is to the detect the B-meson decay vertex position. The PXD is a new subsystem which did not exist in the original Belle experiment. The increased luminosity of SuperKEKB is expected to lead to an increase in the background hit rates by a factor of almost 20 and event rates by

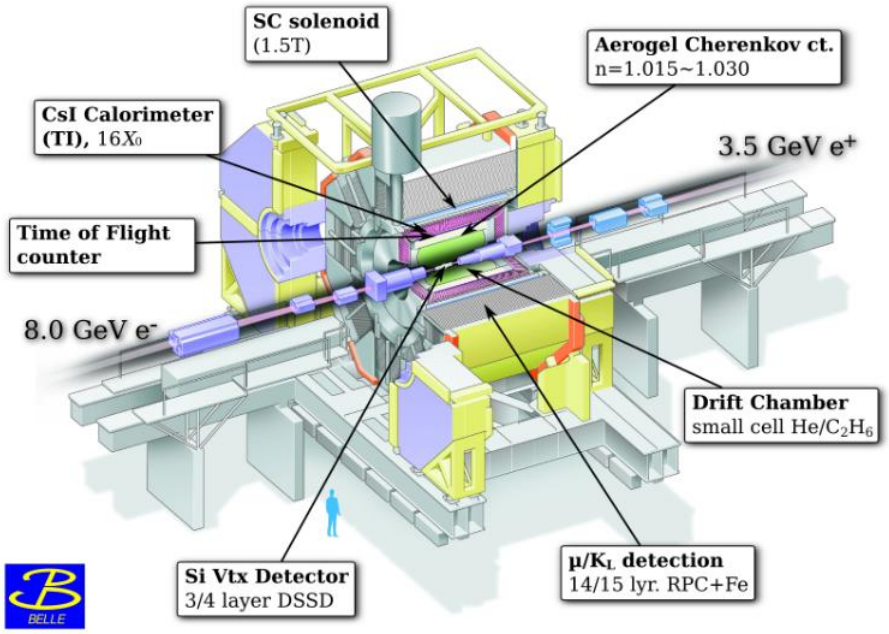

Figure 3.3 – Schematic of Belle II Detector [12].

a factor of 50 [16]. As a result, the vertex reconstruction cannot be done using strip detectors like Belle due to the large occupancy, i.e. the fraction of channels hit in each triggered event, at this proximity to the beam. To address this issue, pixel sensors are used in the inner most vertex detector which have a much larger number of channels and therefore a much smaller occupancy.

As can be seen in figure 3.4, the PXD is organized into a cylindrical geometry and consists of two layers of sensors located at radii of 14 mm and 22 mm respectively. The first layer consists of sensors with pixel sizes of 50 x 50 μm^2 while the second one has 50 x 75 μm^2; these are able to meet the vertex resolution requirement of 20 μm. The sensitive area for the first layer is 80 mm x 15 mm while it is 120 mm x 15mm for the second one; azimuthally this lies between 17° and 150° in the lab frame.

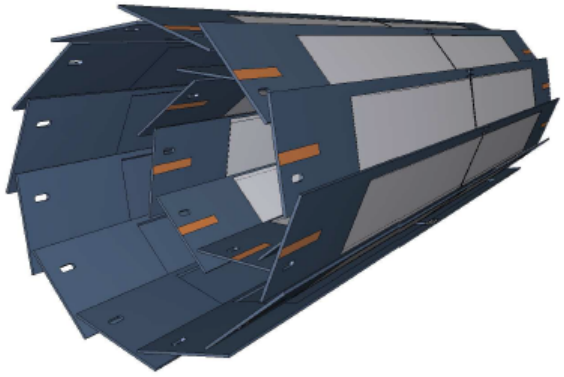

Figure 3.4 – Geometry of the PXD.

PXD in the Belle II experiment is based on the DEPFET (DEPleted Field Effect Transistor) technology which allows for very thin (50 μm) sensors. The DEPFET is a semiconductor detector concept which combines detection and amplification into one device. It consists of a fully depleted silicon substrate and is equipped with a p-channel MOSFET structure with an internal gate. When a charged particle traverses the detector, electron-hole pairs are created which drift towards this internal gate due to the applied voltage bias and are collected. The current generated activates the transistor switch and signals to the readout electronics that a particle has traversed.

The readout electronics are located outside the acceptance region in this design and won't contribute to multiple-scattering as a result. While they need active cooling, air cooling is sufficient for the sensors.The readout electronics are made of three types of Application-Specific Integrated Circuits (ASICs) as shown in figure 3.5. These are the 'Drain Current Digitizers' (DCD), which digitize the MOSFET currents from a row of pixels; the 'Digital Handling Processor' (DHP), which does the zero-suppression of the "empty" pixels; and the 'Switchers' which

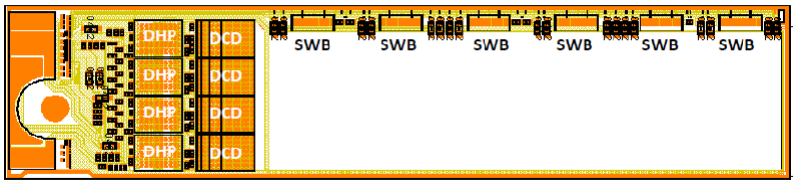

Figure 3.5 – A schematic of the PXD ladder [17].

switch on a pixel row to send the currents to the DCD. While the 'Switchers' are located along a 2mm rim of the PXD ladder on the side of the DEPFET sensor, the DCD and DHP are located outside the acceptance. There are 1600 pixel rows and the processing time for each is about 100 ns; thus all rows can be read in a period of 20 μs.

3.2.2 Silicon Vertex Detector (SVD)

Along with the PXD, the main purpose of the SVD is to measure the vertex location of the two B decays in order to measure the CP-induced asymmetry - one of the main goals of the experiment. The reconstruction algorithms gather information from both the vertex detectors to identify the vertices. The displaced vertex is a result of the asymmetry in the beam energies as discussed earlier; it needs to be measured with an accuracy of $\approx$100 μm.

Particles traversing the SVD have a typical energy of about 1 GeV/c; the vertex resolution is thus dominated by multiple coulomb scattering. As a result, the SVD has to be rigid, low mass and the readout electronics have to be placed outside the tracking region in order to minimze the material [15].

The design of the SVD consists of four layers of double sided silicon-strip detectors (DSSD) as shown in figure 3.6. The layers are slanted in the forward

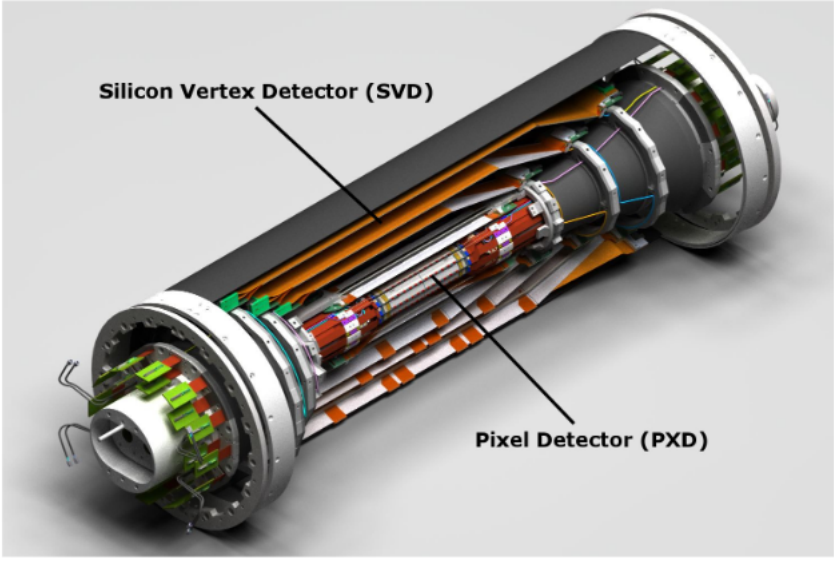

Figure 3.6 – Schematic of the SVD and PXD Detector

direction; this angle reduces the material traversed for the forward going tracks. The innermost layer of the SVD is 20 mm away from the beam line and remainder are 43.5 mm, 70 mm and 88.8 mm respectively. The acceptance offered by the SVD is between 17° and 150° which corresponds to that of the drift chamber [18].

The DSSD is a pn-junction with a bias of 75 V applied on the n-side and is grounded on the p-side; it has a thickness of 300 μm. The diode area of the DSSD is divided into strips with each strip having its own electronic readout. The n-strips are interleaved with p-implants for better electrical separation between them. When a particle traverses the DSSD, it creates electron-hole pairs which then drift towards the corresponding p or n side and produce a two dimensional hit signal as shown in figure 3.7. The p strips are along the beam axis and allow for measuring the $r\phi$ coordinate whereas as the n strips measure the z position. The performance of the SVD is indicated by the resolution of the reconstructed vertex

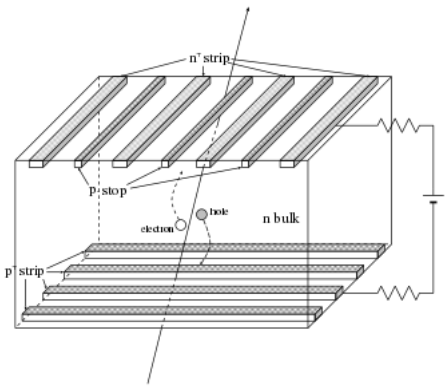

Figure 3.7 – Operation of the DSSD [13].

in the $r\phi$ and z direction which is given by,

$$\sigma_{r\phi} = 22 \oplus \frac{36}{p\beta \sin\theta^{3/2}} \qquad \sigma_z = 28 \oplus \frac{32}{p\beta \sin\theta^{5/2}}, \tag{3.1}$$

where p is the momentum of the particle and $\oplus$ is the quadratic sum [13].

3.2.3 Central Drift Chamber (CDC)

The CDC has three primary roles: it reconstructs the tracks of the charged particle and measures their momentum, it assists with particle identification by measuring the energy loss of particles and it also provides for reliable trigger signals for charged particles.

The design of the CDC consists of a hollow cylinder filled with a gas combination of 50% Ethane and 50% Helium and has three main structural components: a thin carbon-fiber reinforced plastic inner cylinder, two aluminum end plates, and an outer cylinder. It has sense and field wires distributed in its volume; these wires stretch from the forward to the backward support plates with a high tension

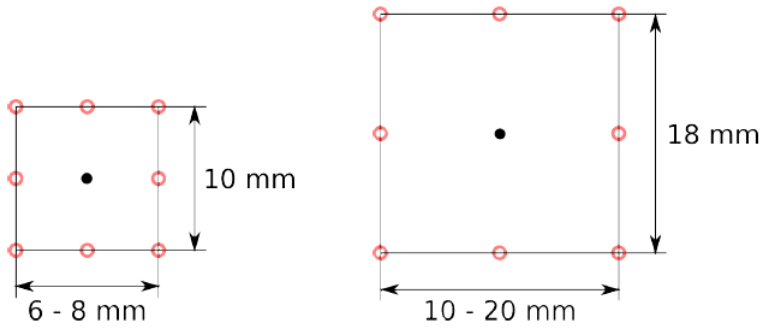

Figure 3.8 – Wire configuration for the field and sense wires inside the CDC.There is one sense wire surrounded by eight field wires. The smaller cells are in the inner part of the CDC while the larger ones are on the outside [19]

.

to minimize gravitational lag. The sense and field wires, as seen along the beamline, are configured in a cell configuration as show in in figure 3.8. In each of these drift cells, a sense wire, made of gold plated tungsten, is located in the middle to collect the charge generated in the cell and is connected to readout electronics at the backward end plate at ground potential. It is surrounded by eight field wires in the cell which shape the electric field and define the boundary to the next cell; a high negative voltage is connected to them to repel the electrons to the sense wires [19].

When a charged particle traverses the CDC, it ionizes the gas in the chamber. The ionized electrons drift towards the sensing wires due to the drift field and ionize additional gas atoms. This creates an electron avalanche and a large electronic pulse is registered as a 2D hit at the sense wire. Hits on the axial sense wires provide $r - \phi$ information while hits on the cathode layers and stereo wires provide z information. The particle's charge and momentum can then be determined based on the trajectory in the magnetic field and the ionization per unit length (dE/dx) is used for particle identification [20] [21].

A super-conducting solenoid provides the 1.5 T magnetic field which surrounds the CDC and TOP, and is aligned parallel to the beamline. As a result of this field, the particle trajectories are bent by the Lorentz force. There are 14336 elementary drift cells in the CDC organized into 56 layers. The subsystem starts at a radius of 160 mm and ends at 1130 mm with an acceptance region that lies between 17° and 150°. The spatial resolution of the CDC is about 100 μm and the resolution on the dE/dx measurements for particles with an incident angle of 90° is around 12% [16].

3.2.4 Particle Identification (PID) Detectors - TOP and ARICH

There are two detectors responsible for particle identification (PID) in Belle II, the Time-of-Propagation (TOP) detector and the Aerogel Ring Imaging Cherenkov (ARICH) detector. These detectors are responsible for distinguishing kaons and pions; the TOP accomplishes this for the barrel region while the ARICH does this in the end-cap regions.

These detectors employ Cherenkov radiation for PID purposes. Cherenkov radiation is emitted by a particle when it traverses a material with a speed faster than the speed of light in that material. The photons emitted form a cone around the particle's track with a characteristic angle which is inversely proportional to its velocity and is given by

$$\cos\theta_c = \frac{1}{\beta n}, \tag{3.2}$$

where n is the refractive index, and β is v/c where v is the particles velocity and c is the speed of light. Since the angle carries information about the particle's velocity, it can be combined with the momentum measurement from the CDC to determine

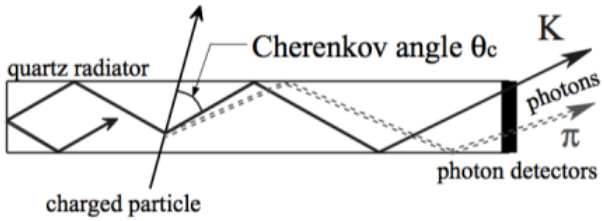

Figure 3.9 – A schematic showing the principle of operation for the TOP.

the mass, and thus identify the particle.

Time-of-Propogation (TOP) detector

The TOP consists of 16 rectangular shaped modules surrounding the outer wall of the CDC forming a cylinder as shown in figure 3.9. Each module is a 2.7m long quartz radiators composed of two quartz bars glued together; they have a transverse area of 4420 mm^2 and a total length of 2500 mm. The readout photomultiplier tubes are located in the backward end of the modules. A mirror at the forward end of the quartz bar reflects back the photons from the forward direction. The required time resolution for a single-photon detection is around 50 ps.

A schematic showing the principle of operation for the TOP is shown in figure 3.9.The angle of the incident Cherenkov photon determines the trajectory of propagation within the TOP module, with different angles producing different path lengths. This angle is inferred based on the time of propagation (TOP) of the light in the detector; the particle velocity can be determined from it which is then used to calculate the likelihood for a mass assignment [16].

Aerogel Ring Imaging Cherenkov (ARICH) detector

Similar to the TOP, the ARICH uses Cherenkov radiation for the purposes of particle identification - except it is used for the end-cap region instead of the barrels. Its main task is to separate kaons from pions and also to provide discrimination between low energy (below 1 GeV/c) pions, muons and electrons.

A schematic showing the main components of the ARICH is shown in figure 3.10. Cherenkov photons are produced by an aerogel radiator as charged particles traverse the detector. The photons form a ring on the photo-detector plane and the angle of the emitted photons is measured directly based on the characteristics (i.e. radius) of the resulting ring. This angle is then use for PID purposes as explained earlier.

There are two layers of aerogel radiator tiles that cover the forward end cap; each is 20 mm thick and has a slightly different refractive index (n_1 = 1.046 and n_2 = 1.056) to ensure the radiation is focused on the photo-detector plane; this is followed by an expansion volume. The readout is done by an array of photon detectors that determine the position and are located 20 cm behind the radiators. ARICH is expected to provide 4σ separation between pions and kaons up to a momenta of 4 GeV/c. The global acceptance stretches from 15° to 30° in azimuth.

3.2.5 Electromagnetic Calorimeter (ECL)

The ECL's main task is to identify and provide high resolution energy information about the particles that interact electromagnetically, namely photons and electrons. It is responsible for detecting them with a high efficiency, determining their angular coordinates, precisely determining their energy, generating the

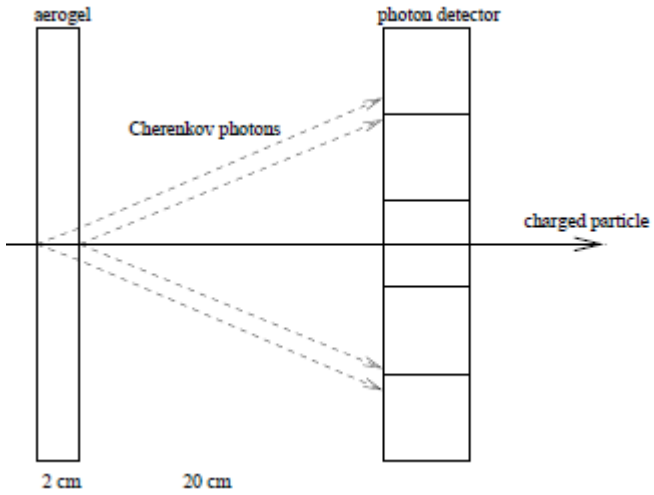

Figure 3.10 – A schematic showing the design of the ARICH detector.

proper signal for the trigger and also helps with the detection of K_L^0 along with the KLM. About one third of the B-decay products are π^0 or other neutral particles that result in photons which range in energy from 20 MeV to 4 GeV; it is thus designed to be versatile and makes up one of the most important parts of the detector.

The ECL is made up of thallium doped cesium-iodide crystals which are divided into the barrel and endcap region. When an electron or photon traverses one of the crystals, it deposits its energy into them through electromagnetic showers produced by Brehmmstrahlung and pair production. As the shower cascade evolves, more particles carrying a lower fraction of the original energy are generated. Below a critical value (≈ 1 MeV), the electrons and positrons lose most of their energy by ionization, pair production thus stops contributing to the shower development which eventually ceases. The crystals are large enough to contain the showers; the light produced by scintillation of the CsI(Tl) crystals is taken to be be proportional to the deposited energy of the incident particle [21].

A schematic showing the calorimeter is shown in figure 3.11. The barrel re-

gion region is 3m in length and has an inner radius of 1.25m; the forward endcap and backward endcaps are located at 1.96m and 1.02m from the interaction point respectively. The azimuthal acceptance is $12.4^\circ < \theta < 155.1^\circ$. There are a total of 8736 CsI(Tl) crystals in the ECL in truncated pyramid shapes with a 6 x 6 cm^2 cross-section and length of 30 cm for the average crystal. The readout is carried out by two 10 x 20 mm^2 photodiodes which are glued onto the crystal by a 1mm plexiglass plate. The average output signal of the crystals gives 5000 photoelectrons per 1 MeV of energy deposited with the average noise level being 200 keV. The higher background rate relative to Belle will be handled with new readout electronics based on the signal sampling method; the crystals and the photo-detectors are being reused from the previous experiment. The intrinsic energy resolution is given by the approximated formula [11]:

$$\frac{\sigma_E}{E} = \sqrt{\left(\frac{.066\%}{E}\right)^2 + \left(\frac{.81\%}{\sqrt[4]{E}}\right)^2 + 1.34\%^2}, \tag{3.3}$$

where E is the energy and the first term is the electronic noise contribution.

3.2.6 K_L^0 and μ Detector (KLM)

The KLM is designed to detect and distinguish muons from long-lived neutral kaons, K_L^0. It is the last subsystem in the detector, located right after the ECL, and sits outside the 1.5 T magnetic field of the solenoid. The detector consists of an alternating sandwich of 4.7cm thick iron plates and active detector elements made of glass electrode resistive plate chambers (RPC) as shown in figure 3.12. The octagonal barrel covers the polar angle range from 45° to 125°, while the endcaps extend this coverage from 20° to 155°. In the barrel, there are 15 detector layers

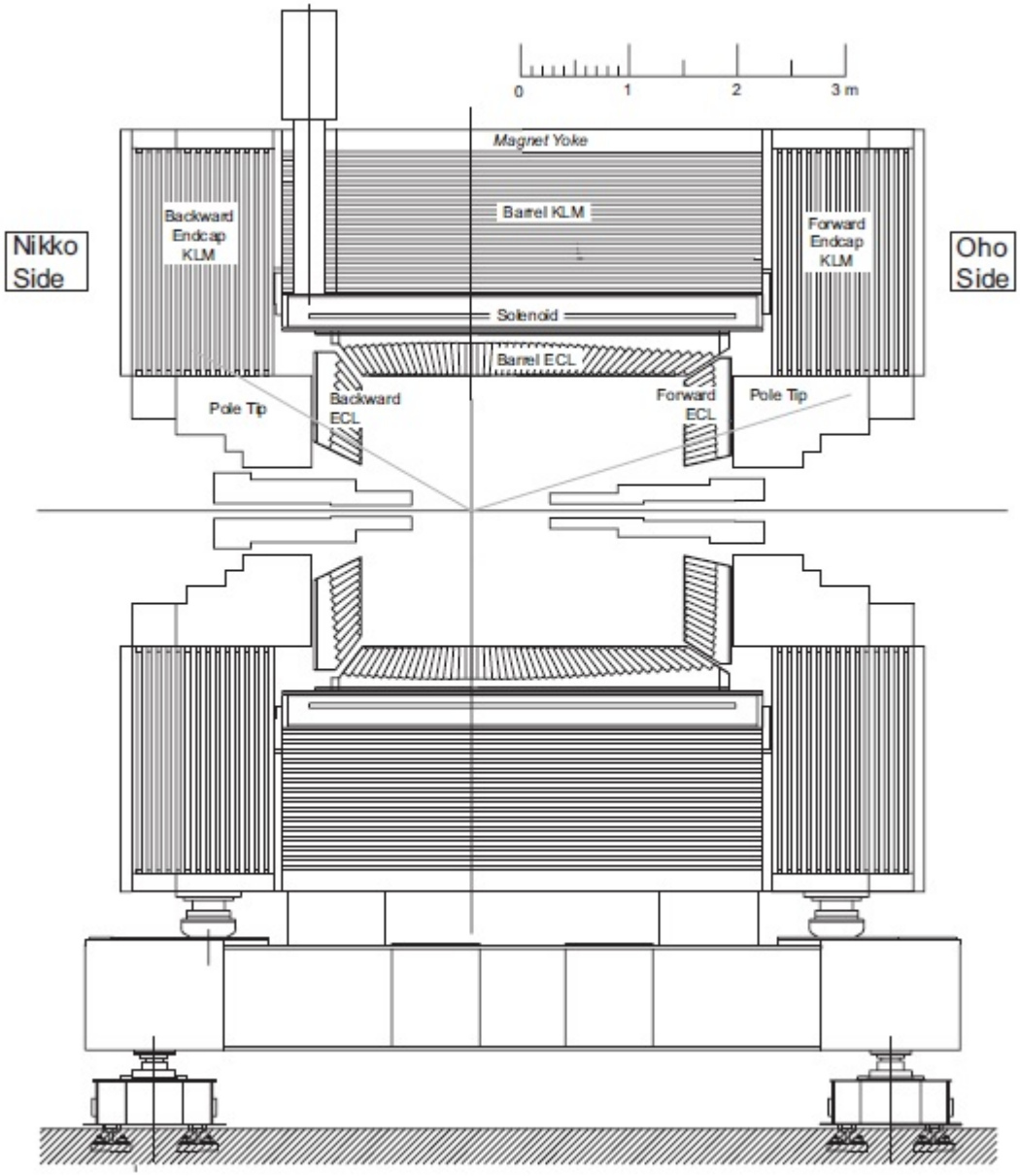

Figure 3.11 – A side view showing the ECL and KLM in the detector.

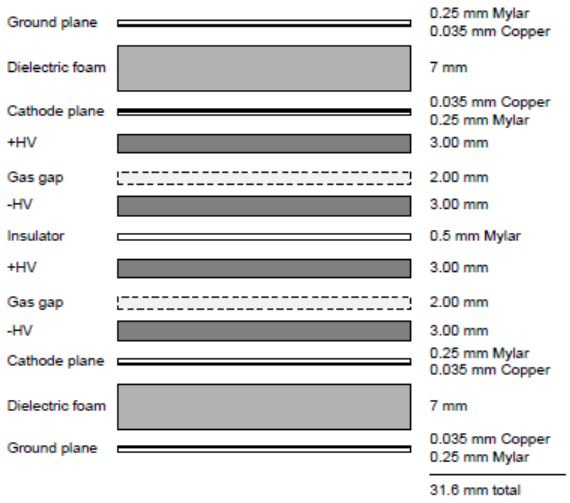

Figure 3.12 – An exploded view of the resistive plate chambers (RPC) in the KLM.

and 14 iron plates, and 14 detector layers and 14 iron plates in each endcap.

K_L^0 and muons can be distinguished based on the pattern they leave behind in the detector. Muons interact electromagnetically, primarily through ionization, and those with a momentum of greater than 0.6 GeV/c travel in nearly straight lines in the KLM until they either escape or range out due to electromagnetic energy deposition. They can be reconstructed using the charged tracking information they leave behind in the CDC. On the other hand, the K_L^0 interacts strongly, doesn't leave tracks in the CDC and produces a hadronic shower which is detected in either the ECL, KLM or both. The signature left behind is thus fundamentally different for the neutral kaons and charged muons.

3.3 Basf2: The Belle Analysis Software Framework 2

The software framework of the experiment is called Belle II Analysis Software Framework (basf2). Its strength lies in being able to carry out both online

tasks (such as a data acquisition and trigger) as well as those offline (such as analysis and reconstruction). C++ is the main language in which the framework is written and it is interfaced with python as a steering language. It relies on GENFIT4 and RAVES for track and vertex fitting respectively. Established third-party libraries such as ROOT, boost, CLHEP and libxml are used throughout the software. This new framework incorporate concepts from other HEP experiments such as LHCb, ALICE and CDF [12].

3.3.1 The basic architecture

Given the large amount of data that will be generated at Belle II, basf2 was designed to process these large datasets in a flexible and configurable way. Thus each data-processing method is designed as a module which can be adjusted by the user. The modules are arranged in a linear order in a container called a path. The user can form a data processing chain by linking together an arbitrary number modules and paths. During the data processing, basf2 executes the modules of a path one at time in the order they are placed in the path. The data to be processed is stored in a common storage called DataStore. A schematic showing this process for a path consisting of four modules is shown in figure 3.13. The tasks of these modules can range from reading data files to creating full detector simulations [22].

3.3.2 Geometry and Simulation

A geometrical description of the detector is needed for all the tools in the offline software chain in the basf2 framework. Starting from Monte Carlo simulations

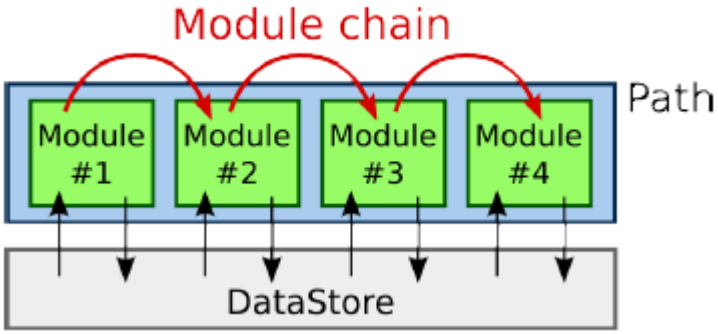

Figure 3.13 – A schematic showing the data processing approach for a path consisting of four modules [22].

of particles traversing the detectors, to simulations of the response of the various subsystem to these particles, to the final reconstruction of the tracks. To ensure all tools in basf2 have access to the same detector description, all the necessary parameter values are stored in a central repository. Using C++ , the geometry used for simulation and reconstruction is created based on these stored parameters. Storing parameters instead of concrete geometry in the central repository allows for the handling of changes in the detector over the course of the commissioning. The simulation for the Belle II detector is based on Geant4 which is the standard in experimental particle physics; basf2 uses the G4Root library for making geometry objects [22].

4

Analysis Techniques

4.1 X/X_0 imaging using high resolution tracking telescopes

Radiation length (X/X_0) imaging is a technique developed to study the material composition of planar objects by constructing high resolution 2D images of the object's radiation length. It is performed by shining a test beam of particles on the object and reconstructing the scattering angles of the particles traversing it; these angles can then be used to extract information about the object's material profile as they are related to the X/X_0. In order to determine the accuracy of the material model in the basf2 simulation, X/X_0 images of the PXD and SVD ladders were compared against the material profile in the simulation; the results of the comparison are detailed in Chapter 5. In this section, a summary of how X/X_0 images are created is given. The images used in this thesis were constructed by Benjamin Schwenker and Ulf Stolzenberg at the University of Göttingen; the information in the section below is extracted from their results given in [23].

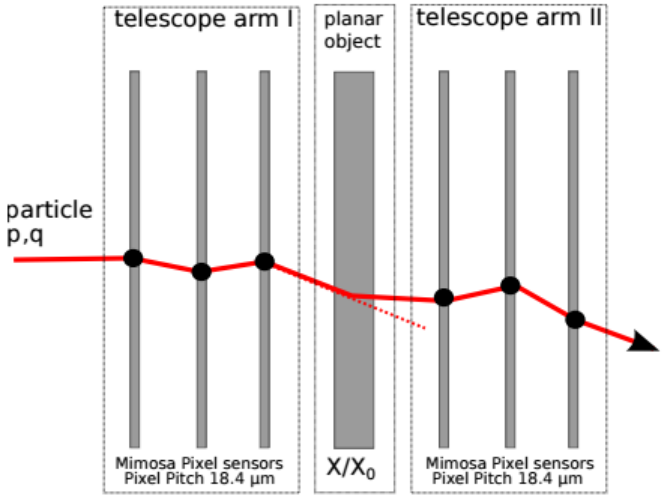

Figure 4.1 – Experimental setup for the creating the X/X_0 images. The object to be measured is centered between the arms of a high resolution tracking telescope perpendicular to the beam axis.The beam consists of the particles with momenta p and charge q [24].

4.1.1 Methodology

To measure the material composition of a planar object, it is placed in the center of a high-resolution tracking telescope as shown in the schematic in figure 4.1. Charged particles from a multi GeV beam are then directed at the object. The main idea is to reconstruct multiple scattering angles from the charged particle tracks on a central measurement plane. A Kalman filter is used to estimate the local track state and the covariance matrix before and after the scattering from the upstream and downstream hits. The scattering angles can then be calculated from the track state and the angular resolution can be determined from the covariance matrix [25].

The scattering angles associated with a set of tracks are grouped into small pixels based on their intersection with the object plane. The radiation length of a particular pixel area on the object is then computed by fitting the measured angle

distribution of that pixel to the following function [23],

$$\begin{aligned} f_{\text{recons.}} &= f_{\text{scatt.}}(\theta) \otimes f_{\text{err}}(\theta, \lambda, \sigma_{\text{err}}) \\ &= f_{\text{scatt.}}(\theta) \otimes \frac{1}{\lambda\,\sigma_{\text{err}}\sqrt{2\pi}} \exp\left(-\frac{1}{2}\left(\frac{\theta}{\lambda\,\sigma_{\text{err}}}\right)^2\right). \end{aligned} \tag{4.1}$$

In this function, $f_{scatt.}$ represents the multiple scattering distribution and is described by theoretical models such as those given by Moliere [26] and Highland [27]. As explained in the theory section previously, these models relate the width of the angular distribution to the thickness of the material and its properties which are effectively given by X_0. The X/X_0 can thus be extracted using this information; images used in this thesis were constructed using Highland's model. The second part of the equation, f_{err}, represents a Gaussian error function due to the finite angular resolution σ_{err} of the telescope. This broadens the final reconstructed angular distribution; the fit function in equation 4.1 is thus a convolution between the theoretical multiple scattering distribution and the Gaussian error function.

For a precise measurement of the X/X_0, it is vital to know the angular resolution of the telescope σ_{err} with as small an uncertainty as possible. σ_{err} introduces systematic errors in the measurements due to effects like telescope misalignment, uncertainties on the telescope sensor resolution and slight deviations in the beam energy. The calibration factor λ is thus introduced in equation 4.1 to tune the angular resolution for a specific experimental setup to $\lambda\sigma_{err}$. The calibration of the telescope is thus a vital part of the measurement as λ is determined in this step; the overall systematic error on X/X_0 is computed by error propagation of the error on λ. As for the statistical errors of X/X_0, they are computed from the fit errors of the single pixels.

For the X/X_0 images used in this study, a 4 GeV electron beam was used at DESY. AIDA tracking telescopes were used; the hit position resolution of the telescope sensors was 3 μm and the calibrated angular resolution $\lambda\sigma_{err}$ was found to be approximately 150 μrad with λ = 1.171$\pm$.003. An example of an X/X_0 image and its corresponding object is shown in figure 4.2.

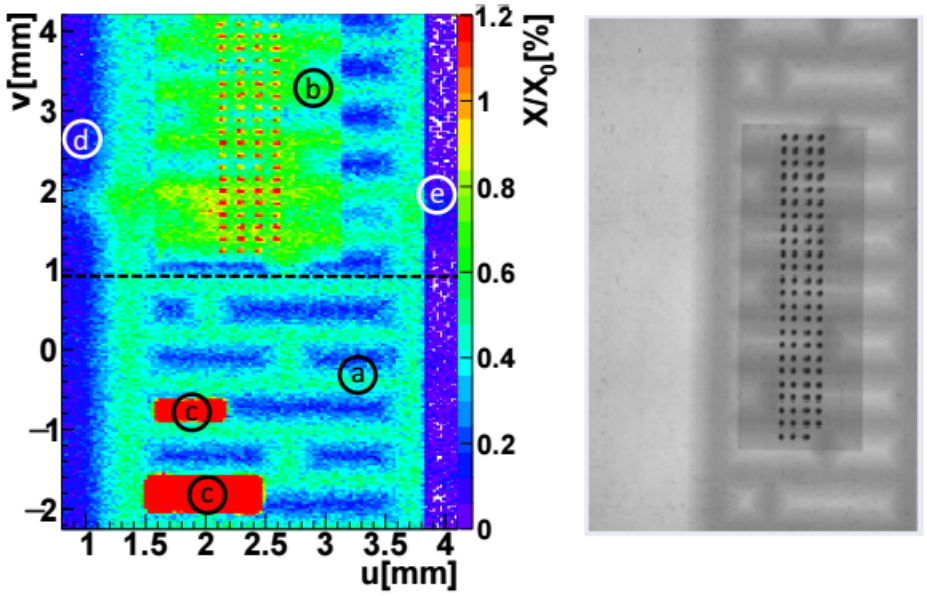

Figure 4.2 – An example of an X/X_0 image generated in the measurements described in [23]. An X-ray image of a section of the PXD ladder is imaged on the right while the corresponding X/X_0 image is on the left.As can be seen, the X/X_0 image captures the alternating groove etches on the ladder and fine details such as the four columns of bump bonds in the switcher. The alphabetical labels identifying the various parts of the image are: (a) groove etches(b) switchers (c) capacitors (d) a 75 μm thin silicon membrane (e) air. Note the X-ray has a smaller field of view and only captures the upper part of the ladder.

4.2 Material Scan tool

The primary means of getting the simulated material profile of the various subsystems in basf2 is through the Material Scan tool. The Material Scan consist of

a 'particle gun' which shoots geantinos around the detector; geantinos are simulated neutral particles that don't interact and undertake the transportation process only. The amount of material they traverse in each step is computed in radiation lengths (X_0) of material and stored in a root tree.

There are two options when running the Material Scan in basf2 - spherical and planar. The spherical scan gives a 2D projection of the detector's material content as viewed by geantinos as they travel outwards from the interaction point; they are distributed uniformly in the polar and azimuthal directions. The input parameters for the spherical scan are: maximum and minimum angles in θ (0° - 180°) and ϕ (0° - 360°), the number of bins for each co-ordinate, and the depth of how far into the detector the geantiono should travel. An example of a spherical scan is shown in figure 4.3.

In the case of a planar scan, the geantinos are created at each point in a specified plane and traverse material in a direction perpendicular to it to give a 2D image of the material seen in that plane. This is useful, for example, to image planar detector structures such as individual sensor boards in the vertex detector. The input parameters for planar scans are: the plane to scan (e.g. xy, yz or custom), the start and end positions for both the axes specified, the numbers of bins in both axes and the depth of the material scan. An example of a planar scan is shown in figure 4.4.

4.2.1 Projection Scripts

While the material scans are useful in obtaining a general qualitative idea of the material in a particular part of the detector, they can be cumbersome to read for more complex parts and are not ideal for detailed quantitative studies. To get

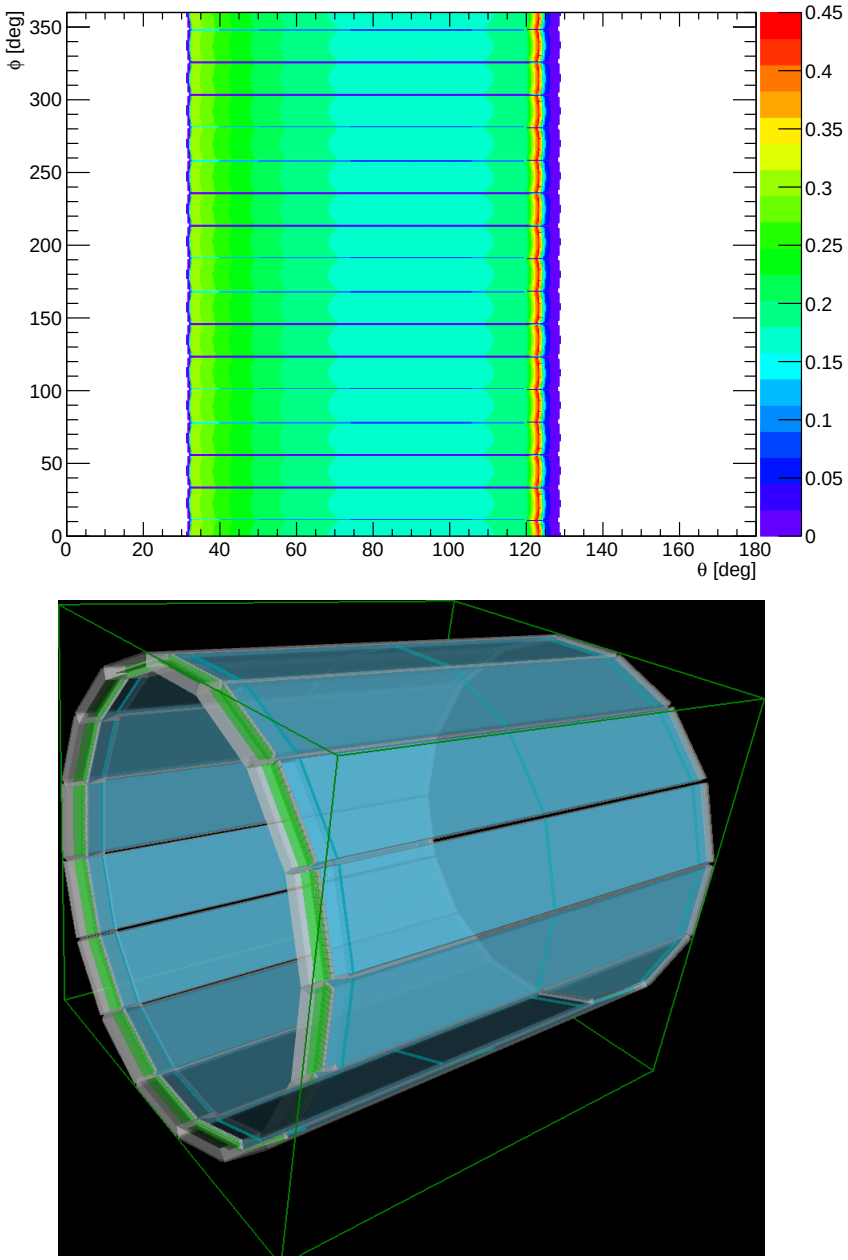

Figure 4.3 – A 2D spherical material scan of the TOP detector (above) and a 3D image of the detector for comparison (below). The plot shows the projection in $\phi - \theta$; it represents the material seen by geantions traversing the detector from the interaction point. The material amount is colour coded and can be interpreted using the legend on the right which represents the material in radiation lengths. For example, green represents about 0.25 X_0 of material.

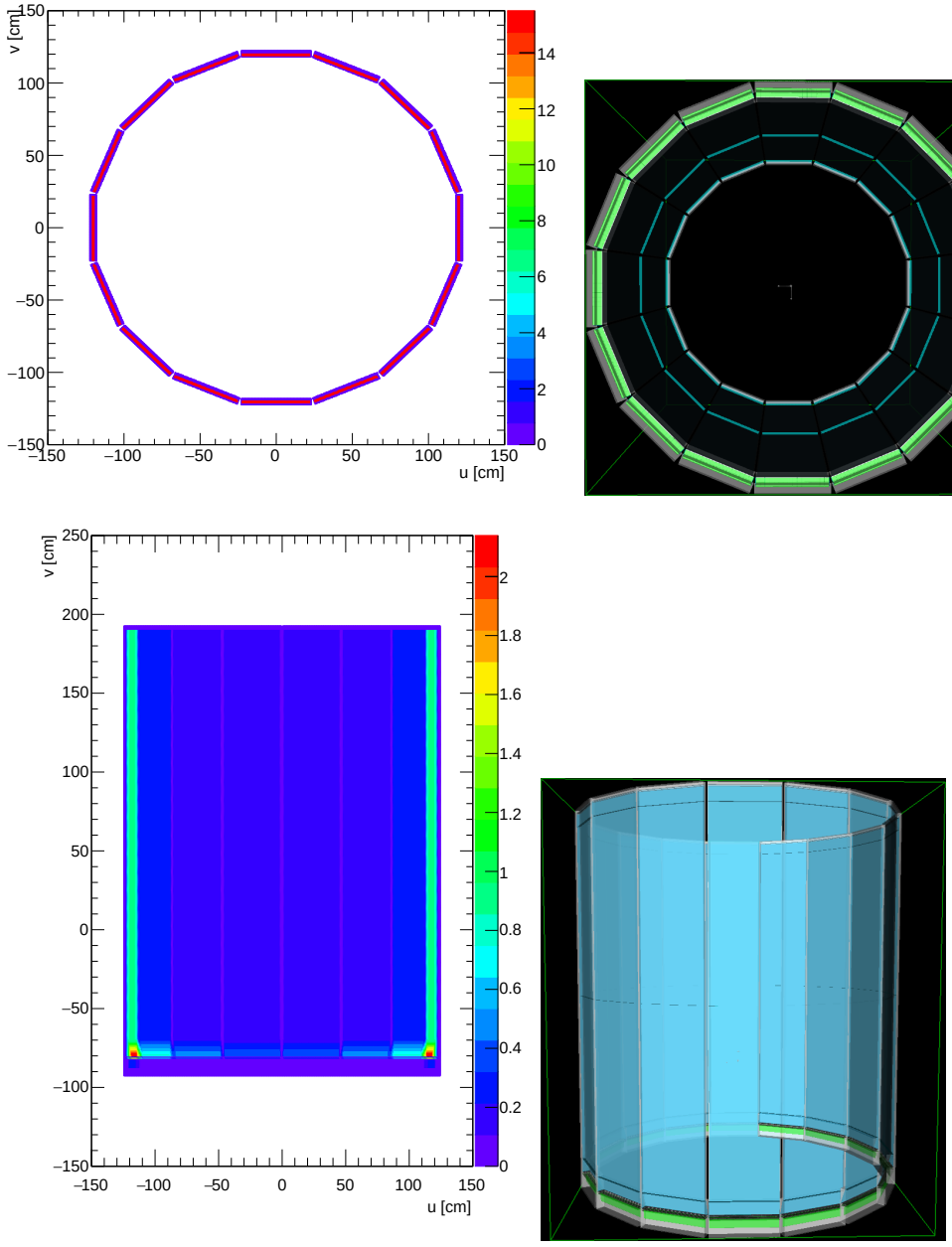

Figure 4.4 – A 2D planar material scan of the TOP detector in the xy (top left) and xz planes (bottom left). 3D images of the detector in the corresponding planes are shown for comparison in the top and bottom right. The plot represents the material seen by geantions traversing the detector perpendicular to the xy and xz planes. Similarly as before, the material amount is colour coded and can be interpreted using the legend on the right of the plots.

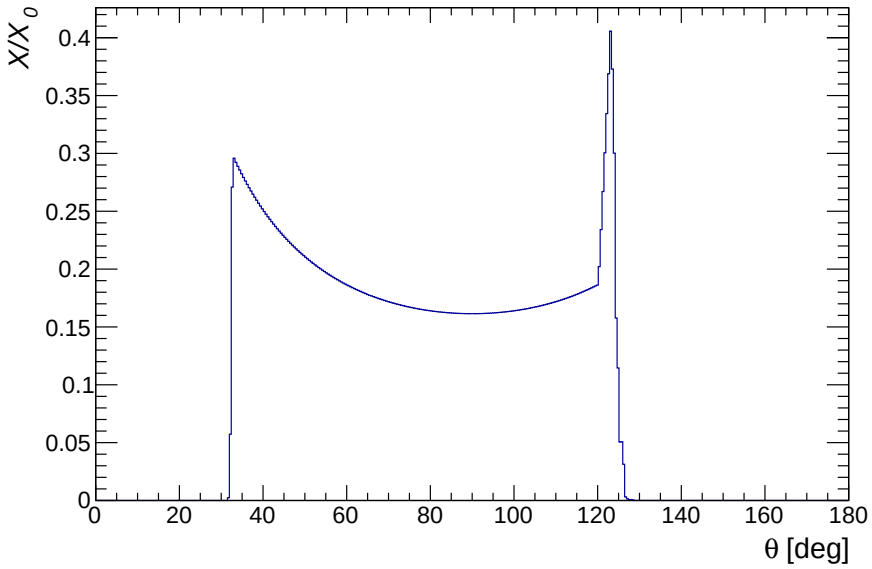

Figure 4.5 – A 1D projection of the TOP detector in θ created by averaging the material in ϕ for the spherical scan in figure 4.3.

a more useful histogram, a macro was used to create a 1D projection from the spherical scans.

An example of the projection in θ for the TOP detector is shown in figure 4.5 which is obtained from the spherical scan in figure 4.3. The plot averages the material content in ϕ and projects it onto the corresponding location in θ.

This plot also shows an important feature to keep in mind when interpreting the spherical scans. The gradient in the profile from the front to the back, corresponding to a decrease from 0.3 X_0 to 0.16 X_0, represents the different amount of material the geantinos 'see'. The physical TOP detector is a linear structure with uniform physical thickness. As can be seen in the 3D image in figure 4.3, the modules making up the TOP structure are made of uniform rectangular slabs. The gradient effect is observed due to the geantinos traversing various lengths based

on the angle at which they strike the material. Thus, the actual physical material in the central region of the TOP module is represented at the 90° point.

4.2.2 Difference Scans

One of the goals of this thesis was to study and document the changes in the material content of the detector between different versions of the software releases. One method of carrying out these checks was by taking two material scans from different releases and then using a macro to take the difference between them and creating a new 2D plot, thus resulting in a 'difference scan'.

An example of a difference scan for the TOP detector is shown in figure 4.6. This was generated by taking the spherical scan shown in figure 4.3 from two different releases and performing a bin-by-bin subtraction. The resulting plot indicates the location and quantity of where material has been added or removed from the detector model between these two code versions. As the colour coded legend indicates in this plot, the green is the area where no changes have occurred, the blue indicates a reduction (negative material) and the yellow is an addition of material (positive material).

When interpreting these plots, it is important to keep in mind that the appearance of the changes in them may not necessarily mean an actual physical change in the material content. It is quite possible that a change in the geometry appears as a change in the material content of the detector. Since the difference scan is comparing the material amount between two regions of space defined by the user, it is possible that a simple shift or rotation in that region appears as an addition or reduction of material. Thus, these difference scans provide information about the geometry changes as well. In order to accurately determine the nature of

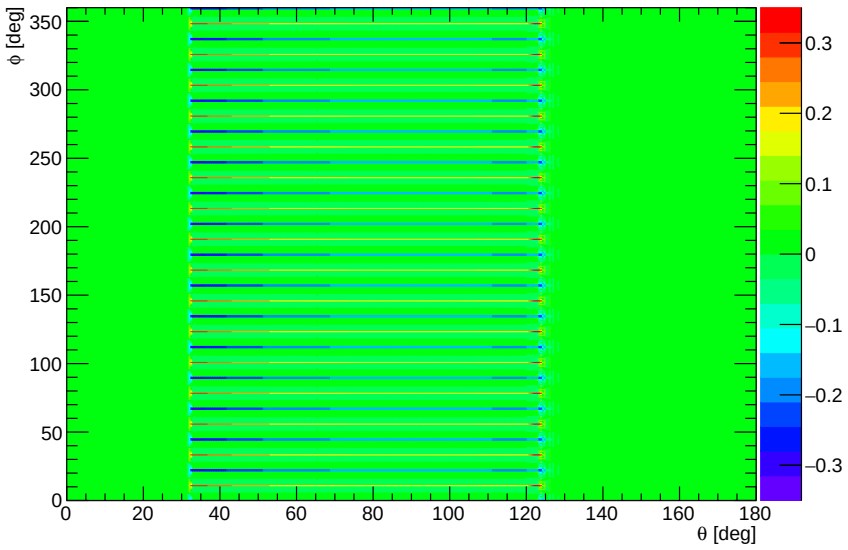

Figure 4.6 – An example of a difference plot generated by taking the spherical scan of 4.3 from two different releases (release-06 and release-08) of the basf2 software. The plots indicate an addition of about 0.2 X_0 (indicated by the yellow lines) and a reduction of 0.2 X_0 (indicated by the blue lines). The change appears in the central region of the TOP detector due to a rotation in ϕ of half the module width, which is appearing as a small increase in material.

the change, further investigation needs to be made by looking at the source code of the detector to determine what was changed in the simulation.

4.2.3 Aliasing Effects and Errors

The computation of the radiation length by the Material Scan tool does not have a statistical uncertainty associated with it as it is not a measurement. The scans represent the physical sum of the material encountered by a single geantino following a specific trajectory and there is nothing random about it; if one runs the simulation a 100 times, one would get numerically identical results each time. Thus, the values for the material content in the detector simulation are exact.

One potential source of error, however, can result due to aliasing effects introduced by the Material Scan. As mentioned earlier, the Material Scan works by computing the cumulative material along the trajectory of a single geantino. More specifically, the final image is constructed by calculating the material seen in the geometric center of each specific bin of the 2D grid. While it doesn't give the average material in each bin, the assumption is that the center of the bin is a good approximation as there is little deviation in material thickness of the bin's area given the large number of bins in each scan ($\approx$ 500x500).

However, it is possible that there might be structures smaller than the bin size which might cause some deviation in the material thickness of the bin area. For example, it is possible that the center of the bin happens to lie in a region with a gap in the structure and the scan thus reports zero material for that bin; this is particularly a concern for structures with a periodic structure. In addition, varying the starting position of the scan can also give different results for such structures.

To demonstrate the impact of aliasing effects as an example here, a number of material scans were generated for the TOP detector (given its periodic structure) and the bin size for each scan was varied. The bin sizes were 500, 493 and 1000; the 500 case is the standard which represents most scans in this thesis.

Figures 4.8, 4.7 and 4.9 show scans with bin sizes (n) of 500, 100, and 493 respectively; figure 4.10 represents a scan with the standard bin size of 500 but with a shifted start of $\theta = 0.3^\circ$ as opposed to 0° like in all other cases. The last case of the shifted start is to see the impact of a shifted geometric center for the bin configuration. As was seen in the 3D image of the detector in figure 4.3, the scan represents the rectangular TOP modules which are joined together to form the detector. The aliasing affects can be observed in the horizontals lines which

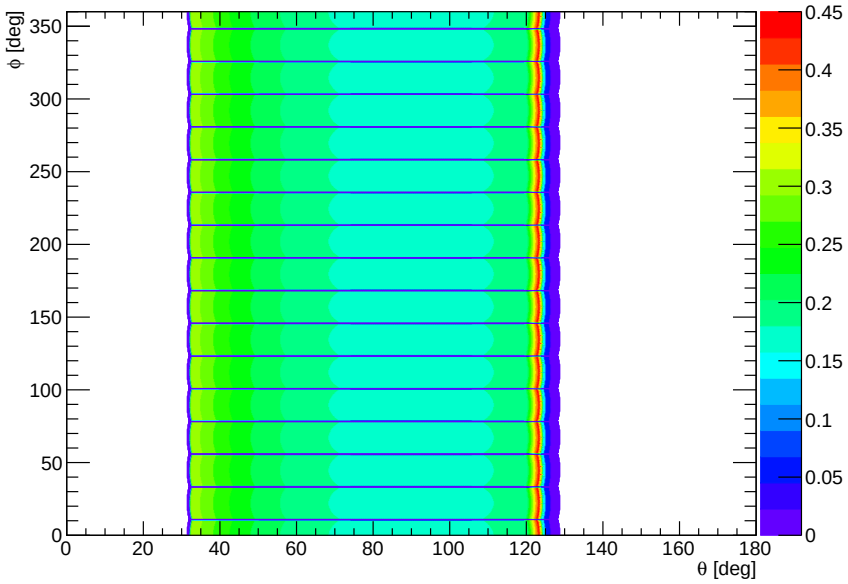

Figure 4.7 – A material scan of the TOP detector with bin size of 1000. The periodic structure represents the modules seen in figure 4.3. The horizontal purple lines indicate the spacings between each module.

represent the gap between the modules. For example, figure 4.7 clearly shows all the horizontal lines between the module due to its high resolution of 1000 bins, while the remainder of the scans do not completely capture this information. In particular, looking at $\phi \approx 125^\circ$, one can see the horizontal lines missing in figure 4.9 and 4.10, but they are visible in the other two scans. When interpreting these plots, it is thus important to verify the scan with the geometry implementation of the detector or one could misinterpret them and assume that there are missing structures in the simulation.

As will be see in Chapters 5 and 6, the quantitative analysis for the material studies will be conducted by applying the projection scripts on the material scans. To determine if the aliasing affects the material content seen in these projections which average over all the bins, figures 4.11, 4.12 and 4.13 were generated; these

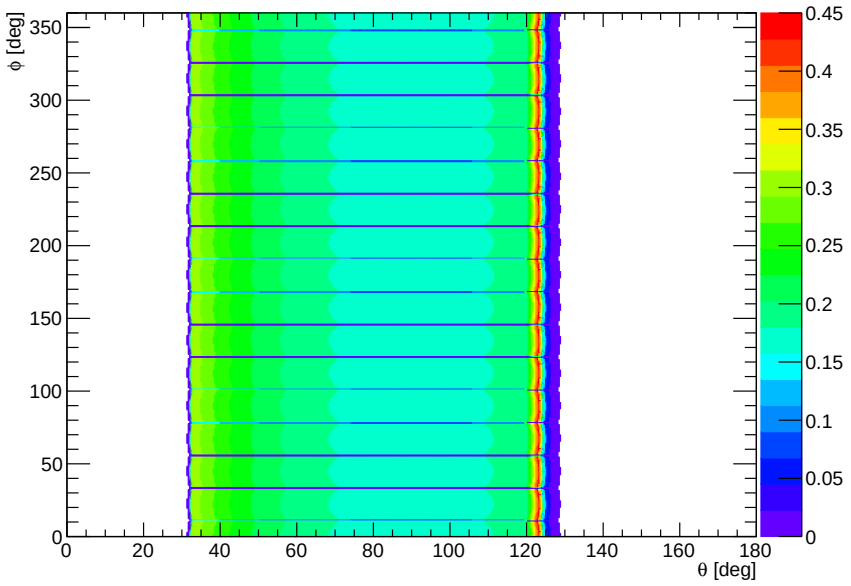

Figure 4.8 – A material scan of the TOP detector with bin size of 500. Compared to figure 4.7, it can be seen there are fewer horizontal lines; this is a result of the lower resolution due to the lower quantity of bins.

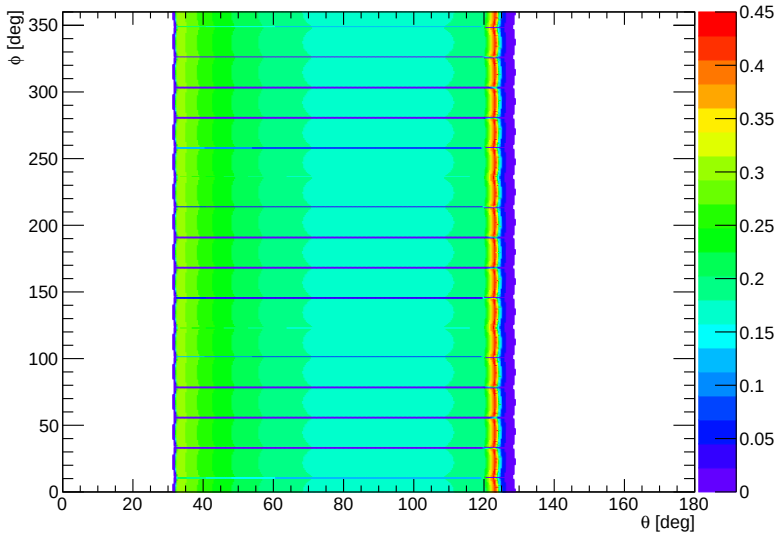

Figure 4.9 – A material scan of the TOP detector with bin size of 493. Compared to figure 4.8, it has a similar number of horizontal lines as they both have almost the same resolution. However, these lines appear shifted or blurred in places due to aliasing effects. For example, at the $\phi \approx 125°$ there is no horizontal line while this is captured in figure 4.8.

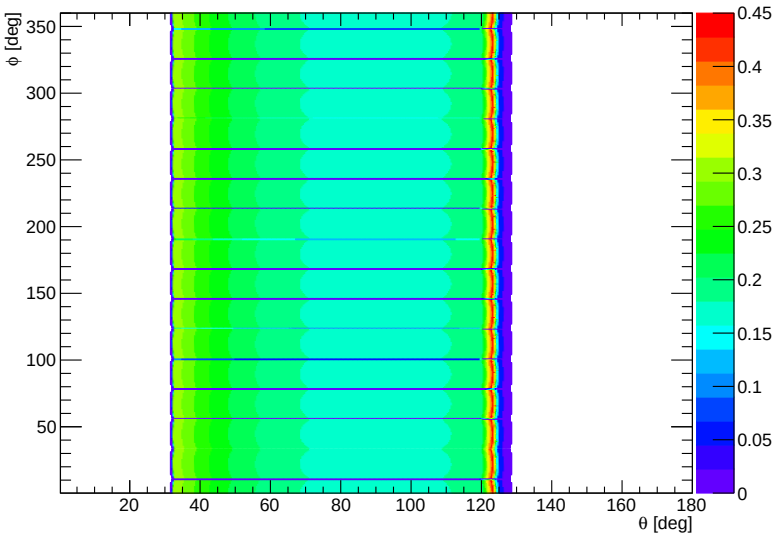

Figure 4.10 – A material scan of the TOP detector with a bin size of 500 but with shifted started position of $\theta = 0.3°$ as opposed to $0°$. The aliasing effect due the shift in starting position is evident here as there are fewer horizontal lines compared by to figure 4.8 despite the same resolution.

compare the material seen in the scan with a bin size of 500 to all the other ones. As can be see in all the projection plots, no differences are observed in the material content when it is averaged over the ϕ direction in these plots. Thus, while the impact of aliasing effects was studied for this thesis, the plots were constructed with special attention to avoid these effects and their impact on the uncertainty of the material scans was treated as negligible.

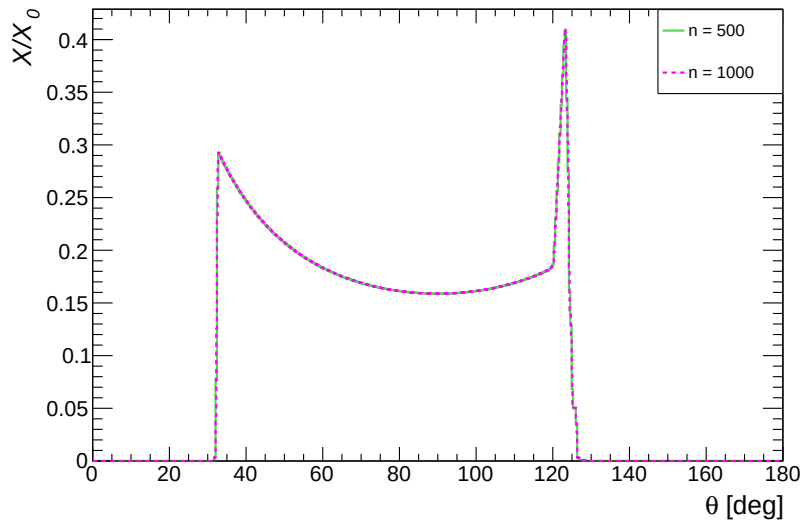

Figure 4.11 – A projection of the spherical scan for the TOP onto θ with the bins averaged in ϕ. Projections from scans with bins (n) of 500 compared with 1000 bins; no deviation is observed in the material content.

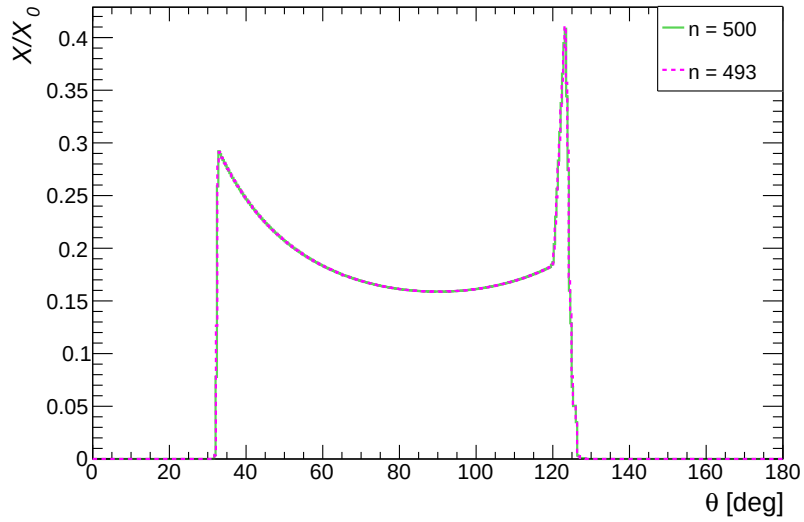

Figure 4.12 – A projection of the spherical scan for the TOP onto θ with the bins averaged in ϕ. Projections from scans with bins (n) of 500 compared with 493 bins; no deviation is observed in the material content.

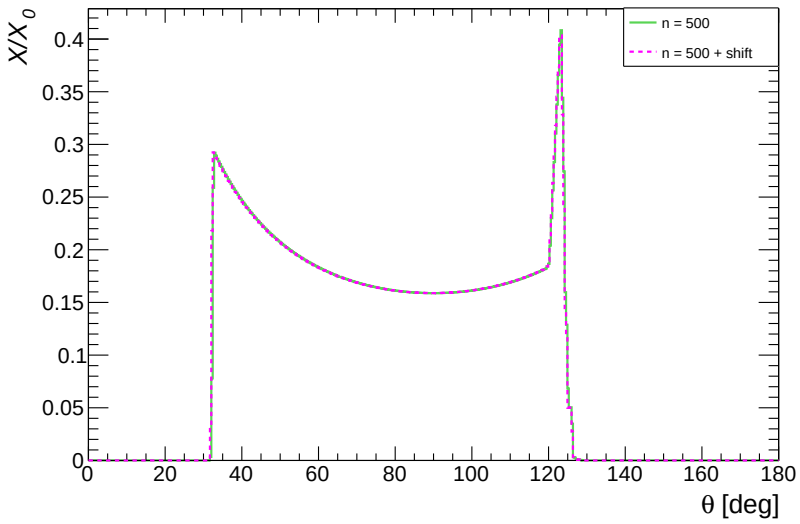

Figure 4.13 – A projection of the spherical scan for the TOP onto θ with the bins averaged in ϕ. Projections from scans with bins (n) of 500 with a start position of $\theta = 0°$ compared with a scans with a start at $\theta = 0.3°$; no deviation is observed in the material content.

5

Precision material studies for the PXD and SVD using X/X_0 imaging

This section summarizes the work done to improve the material model for the PXD and SVD ladders. The radiation length (X/X_0) images are compared with the material model in release-06 of basf2 and the improvements made to the model are highlighted; these changes are scheduled to appear in release-10 of the software which is to appear in the latter half of 2017. A detailed description of the SVD and PXD geometry can be found in Chapter 3; a description of the measurement technique for the X/X_0 images is in Chapter 4. These studies were conducted in collaboration with Benjamin Schewnker and Ulf Stolzenburg at the University of Göttingen.

5.1 PXD Studies

5.1.1 Comparison of X/X_0 images with Basf2

The X/X_0 image of the balcony section of the PXD ladder is shown in figure 5.1; a material scan of the same section taken from the basf2 simulation is shown in 5.3. As per the schematic shown in figure 5.2, the main components visible here are the switchers and capacitor in the balcony region. The shades of darker and

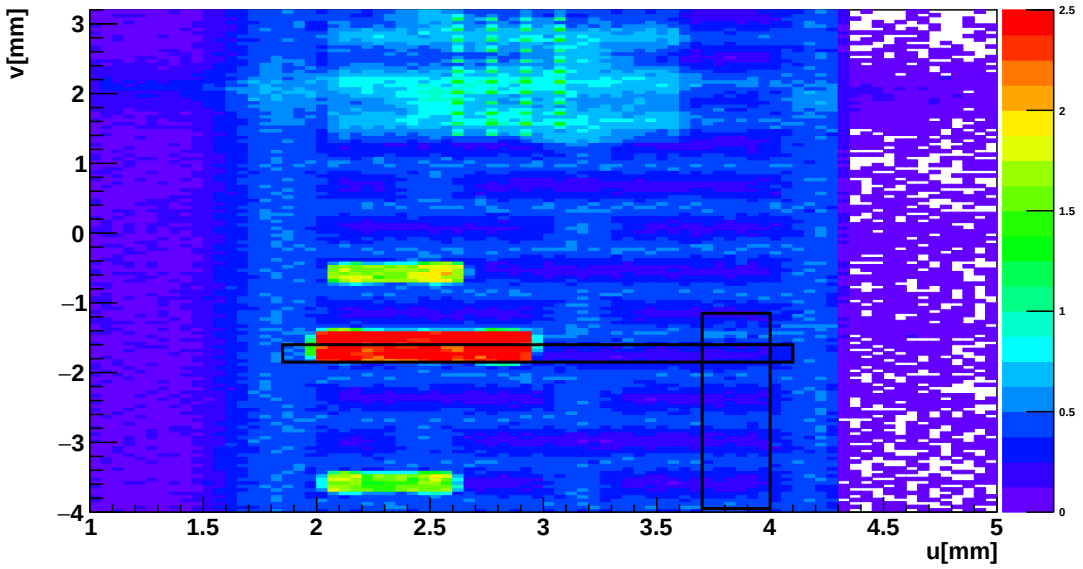

Figure 5.1 – Radiation length image of the a section of the PXD ladder showing the capacitors, switchers and groove profile in the balcony region. The legend on the right represents the amount of material in X/X_0 [%]. The black boxes indicate the cuts for the u and v projections shown in figure 5.4 and 5.5.

lighter blue indicate the groove profile in the ladders which is discussed in more detail below.

Similar amounts of material are observed in both the material scan and X/X_0 image. There is about 0.25 % of a radiation length of material in the sensitive region and 0.75 % in the switchers. The main differences are as follows: missing capacitors, no groove profile in the balcony region and details such as the bump bonds in the switchers are also missing.

To get a more precise estimate of the material in these images, projections in the u and v direction were made in the regions highlighted by the black boxes shown in figure 5.1; these are plotted in figure 5.4 and 5.5. The u and v axes are orthogonal and define a plane which is parallel to the plane being scanned. The

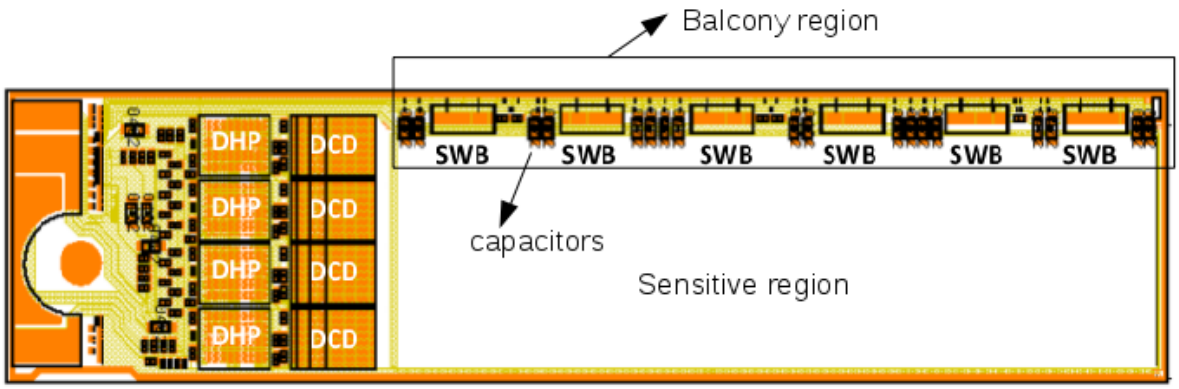

Figure 5.2 – A schematic of a full PXD ladder which shows components of the ladder that are depicted in figure 5.1. The balcony region, capacitors, sensitive region and switchers (SWB) are shown here.

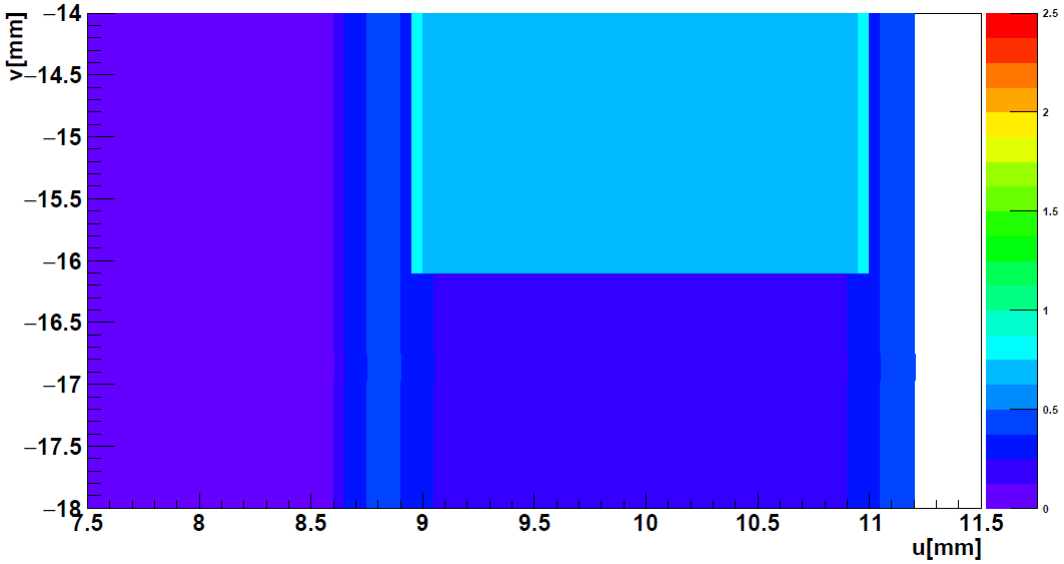

Figure 5.3 – A planar material scan from the simulation showing the same section of the PXD ladder as figure 5.1.

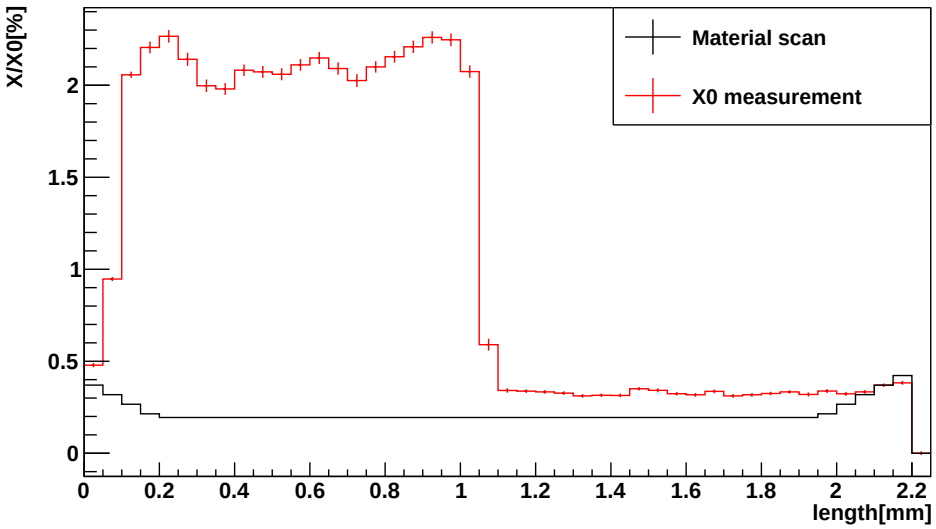

Figure 5.4 – A projection of figure 5.1 in the u-direction showing the differences in the material profile of the simulated and measured PXD ladders. This image highlights the impact due to the missing capacitor in the balcony.

macros used to get these plots average over the rows in each of the black boxes and project the value at the corresponding point.

The u-profile in figure 5.4 shows that the missing capacitor leads to a 1.5 % material difference. There is also a mismatch of about 0.2% material in the base material in the balcony region. The v-profile in figure 5.5 indicates the differences arising due to the missing groove profile; this leads to a difference of 0.5% at the peak of the groove.

5.1.2 PXD geometry improvements

To address the discrepancies uncovered in the previous part, the geometry simulation for the PXD was modified. The resulting improvements made to the material model are shown in figure 5.6. As can been seen, new capacitors have

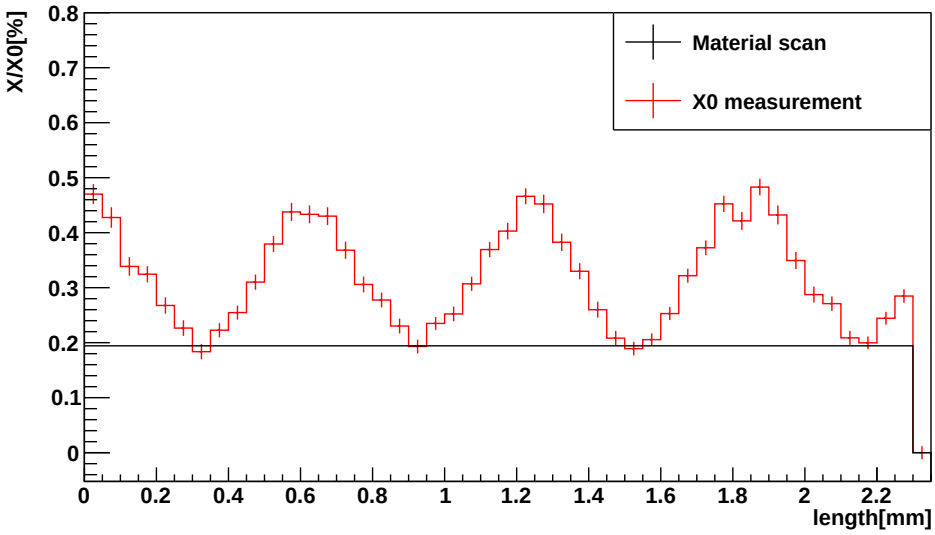

Figure 5.5 – A projection of figure 5.1 in the v-direction showing the differences in the material profile of the simulated and measured PXD ladders. This image highlights the difference due the missing groove profile in the geometry

been added and the material has been etched out in the balcony region to create a groove profile. Projections in the u and v direction are shown in figures 5.7 and 5.8. As can be seen, the 1.5 % difference due to the missing capacitor has now been largely removed. There was also an addition of a 3μm copper layer in the balcony and the thickness of the silicon was changed from 420μm to 525μm. This explains the 0.25% increase in the base which is observed in figure 5.7. Lastly, the addition of the groove profile means the material difference is now at 0.1 % compared to 0.5 % before at the peaks.

The small residual differences seen will remain since the goal here is not to simply match the measurement and simulation. The specifications for the parts added to the simulation come from design documents; the goal is thus to model the simulation as accurately as possible according to the engineering design and

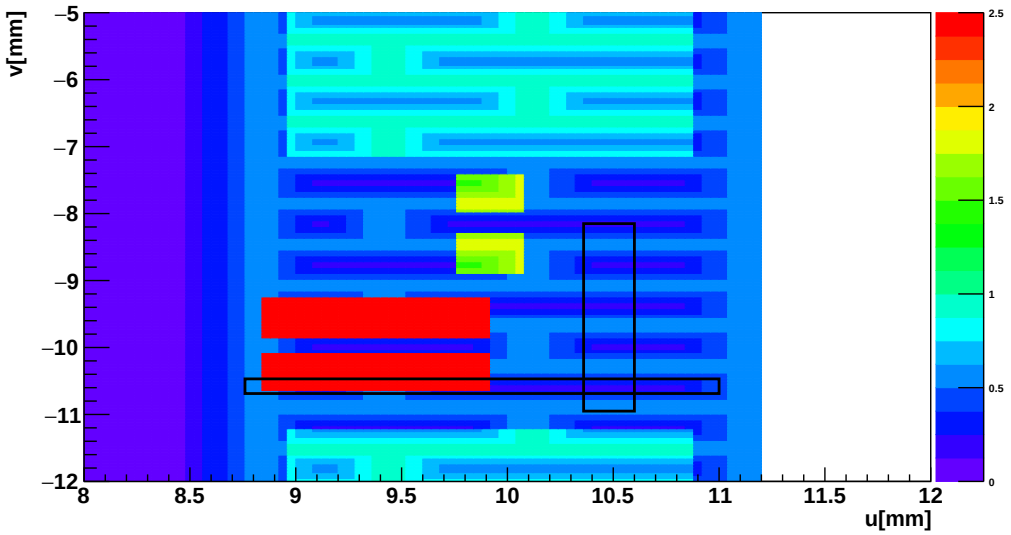

Figure 5.6 – A planar material scan from the simulation with the improved simulation for the PXD ladder. The new capacitor and groove profile can be seen; the black boxes indicate the cuts for the u and v projections shown in figure 5.7 and 5.8.

understand how this design compares to the measurement.

It should also be noted that the location and size of the capacitors in the material scan model do not match the radiation length image completely. This is because the test beam measurements were made on a dummy module where the capacitors were glued on manually and thus not in a very accurate location. Their location and dimensions in the simulation is thus modeled as per the information laid out in engineering drawings.

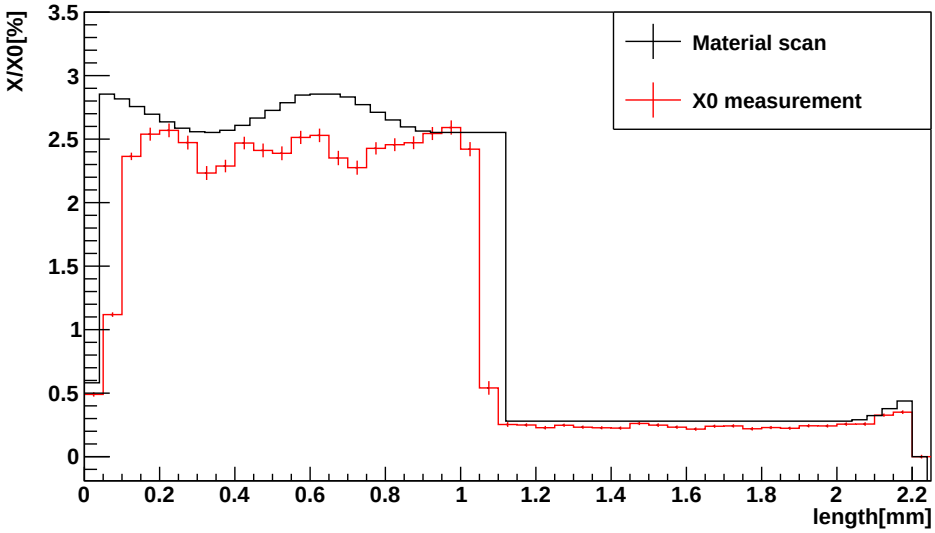

Figure 5.7 – A projection of figure 5.6 in the u-direction showing the differences in the material profile using the improved simulation. The plot depicts the changes due to the new capacitor.

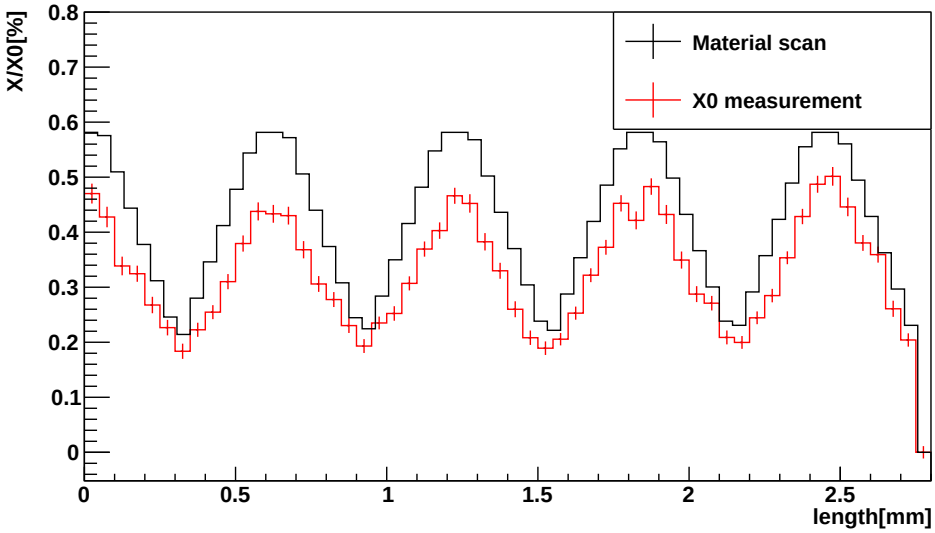

Figure 5.8 – A projection of figure 5.6 in the v-direction showing the differences in the material profile using the improved geometry. The plot depicts the changes due to the addition of the groove profile.

5.2 SVD Studies

5.2.1 Comparison of X/X_0 images with Basf2

Similar to the PXD, the X/X_0 image and a material scan of a section of the SVD ladders is depicted in figures 5.9 and 5.11 respectively. The black boxes in the images indicate the location where cuts were applied for the u and v projections. Figure 5.10 is a photographic image of the same section of the SVD ladder highlighting the components of interest for this study: the cooling pipe, keratherm (a thermal conductor), APV chip (a readout chip) and a clamp which holds the pipe.

As these images indicate, there are several differences between the X/X_0 image and the material scan. Projections in the u and v direction give more details in figures 5.12 and 5.13. As the u-profile shows, there is a difference of 1% of a radiation length of material in the cooling pipes due to a mismatch in the pipe dimensions, the missing keratherm leads to a 0.5% difference and the base of the ladder differs by 0.1%. There is also a misalignment between the two support ribs which appear in the material scan. The gradient observed next to the left support rib is due to some glue added to keep the ribs of the sample ladders in place during the measurements; it thus does not represent the profile of the actual ladders. The v-profile in figure 5.13 indicates that the missing clamp leads to a difference of 0.6% material. In addition, there is a mismatch in the base material of about 0.1% on average which was also seen in the u-profile.

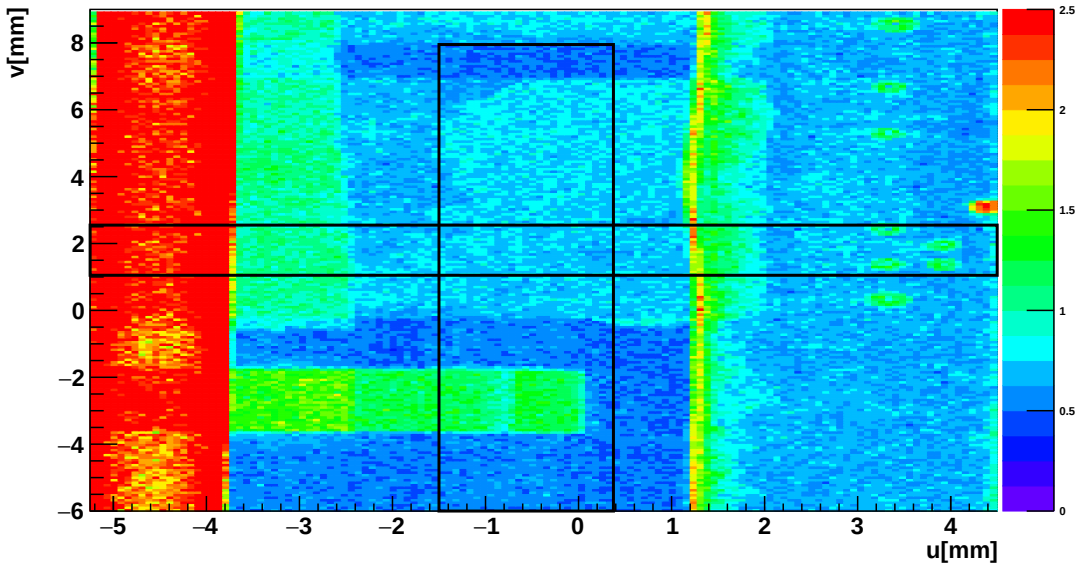

Figure 5.9 – Radiation length image of a section of the SVD ladder showing the cooling pipe, clamps and APV chips as depicted in figure 5.10. The legend on the right represents the amount of material in X/X_0 [%]. The black boxes indicate the cuts for the u and v projections shown in figures 5.12 and 5.13.

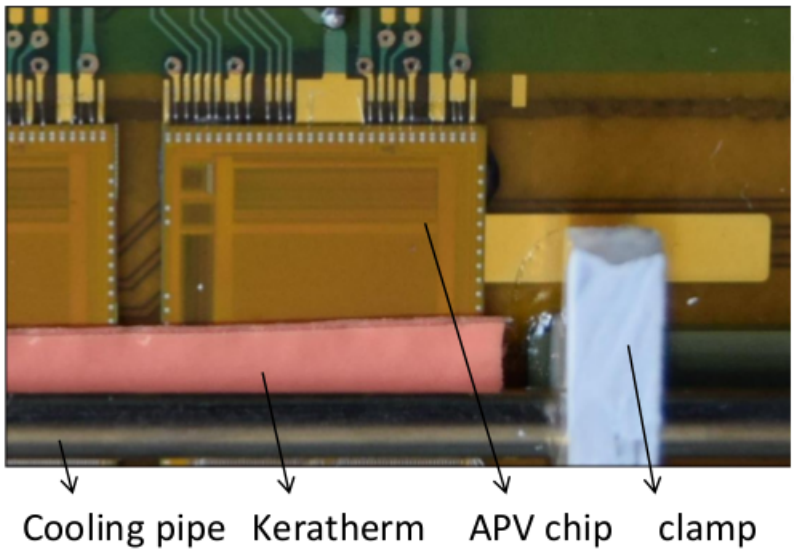

Figure 5.10 – Photographic image of the section of the SVD ladder shown in 5.9; the image is rotated compared to the X/X_0 image.

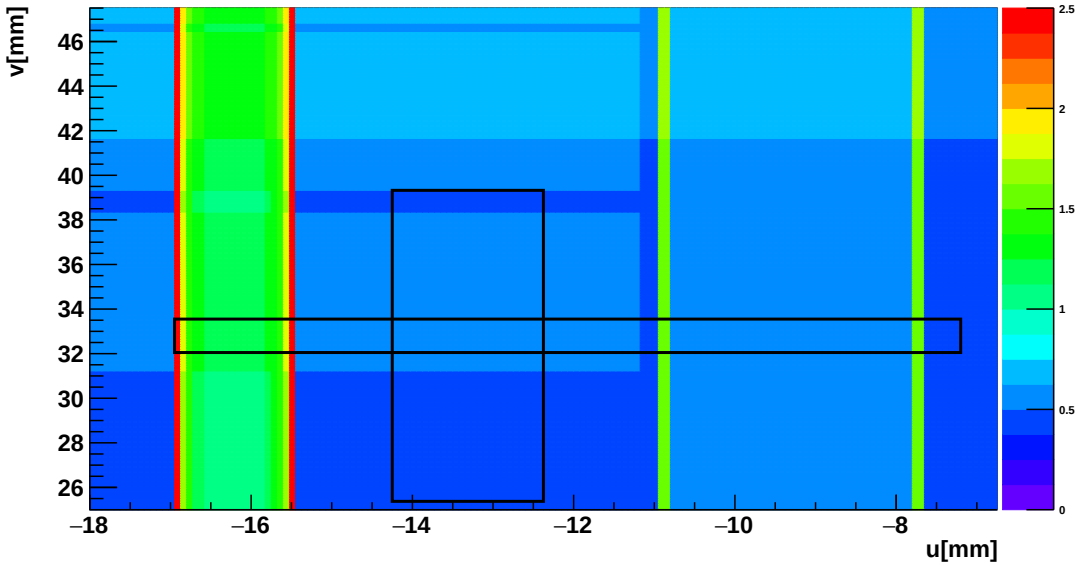

Figure 5.11 – A planar material scan from the simulation showing the same section of the SVD ladder as figure 5.9.

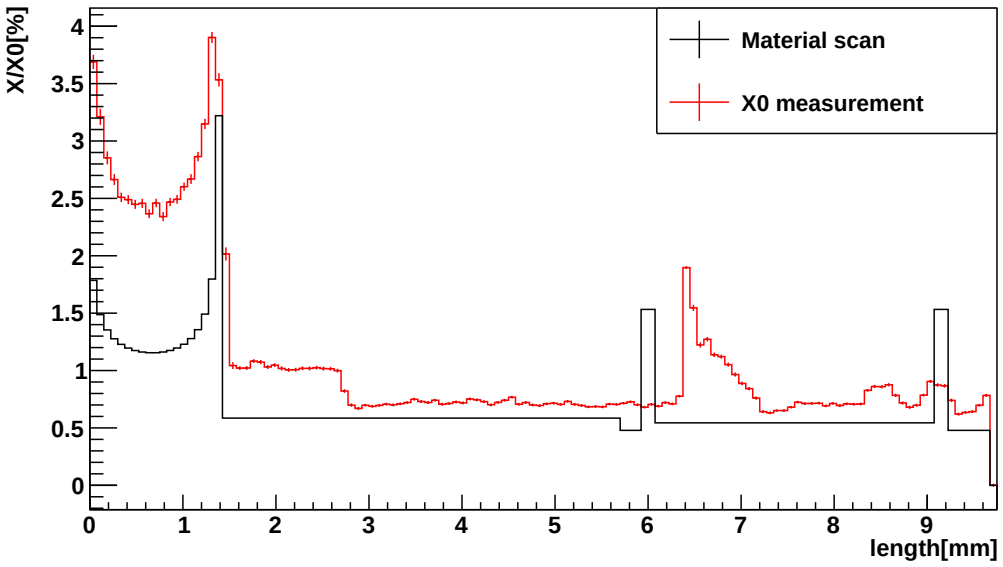

Figure 5.12 – A projection in the u-direction showing the differences in the material profile of the simulated and measured SVD ladders.

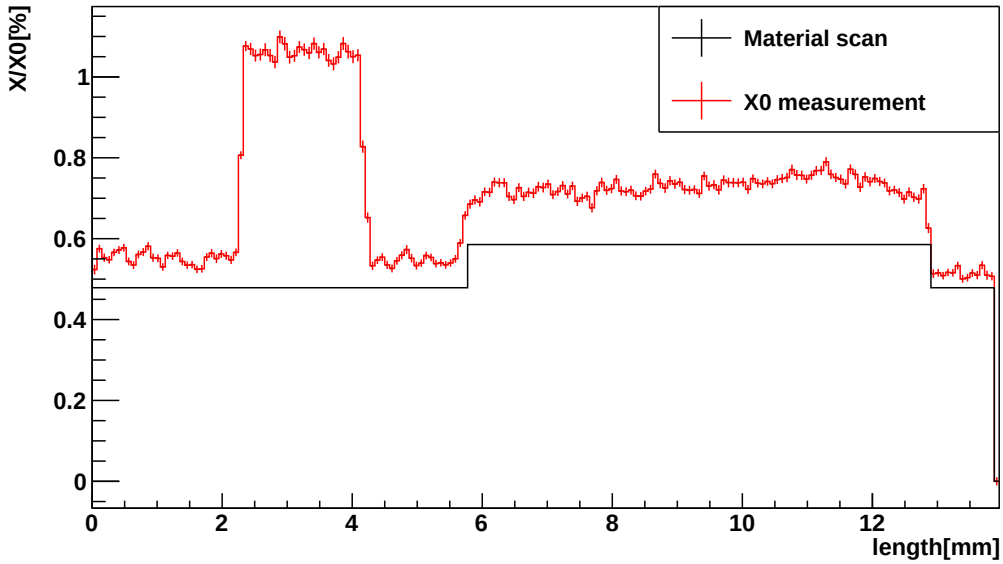

Figure 5.13 – A projection in the v-direction showing the differences in the material profile of the simulated and measured SVD ladders.

5.2.2 SVD geometry improvements

Similar to the PXD, the geometry of the SVD was modified to address the findings of the previous section. The improvements made to the material model are shown in the scan in figure 5.14; the author of the thesis (WA) was primarily responsible for implementing these modifications. As can be seen, a new keratherm layer and a clamp have been added. There was also an addition of a 0.5 mm copper layer under the APV chips which explains the overall increase in the base material.

The u and v profiles in figure 5.15 and 5.16 give more details about the changes to the model. The u-profile indicates the material difference in the cooling pipe has been reduced substantially due to the wall thickness changing from 50 μm to 100 μm; the material difference now sits at 0.2% of radiation length. The addition of the keratherm has also removed the difference of 0.5% observed earlier.

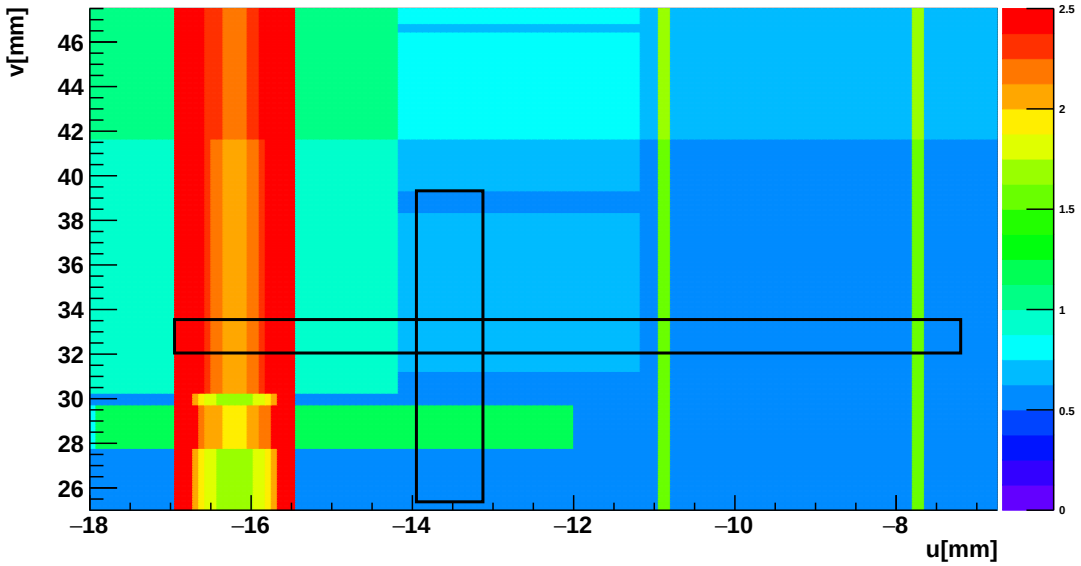

Figure 5.14 – A planar material scan from the simulation with the improved simulation for the SVD ladder.

Finally, the addition of the copper layer has corrected the 0.1% difference that was observed.

The v-profile shows that the addition of the clamp is the biggest observable difference and corrects the 0.6 % discrepancy observed earlier. The addition of the copper layer has also corrected the 0.1% difference found in the base line.

The difference in the location of the support ribs still remains. This was not aligned with the radiation length image because the test beam measurements were made on a dummy module where the support ribs were added manually and thus not very accurate. The location in the simulation is thus modeled as per dimensions laid out in engineering drawings.

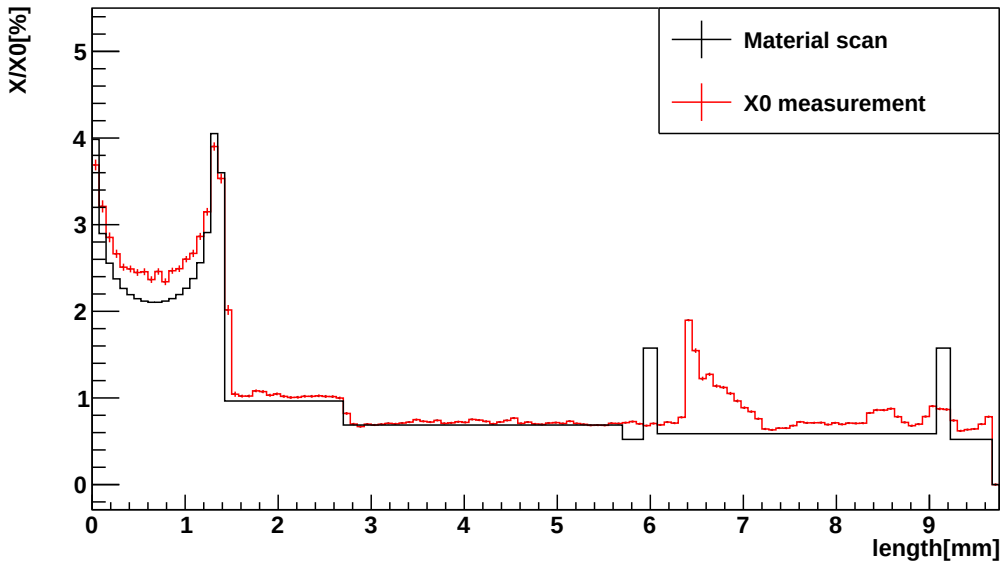

Figure 5.15 – A projection in the u-direction showing the differences in the material profile of the simulated and measured SVD ladders after improvements.

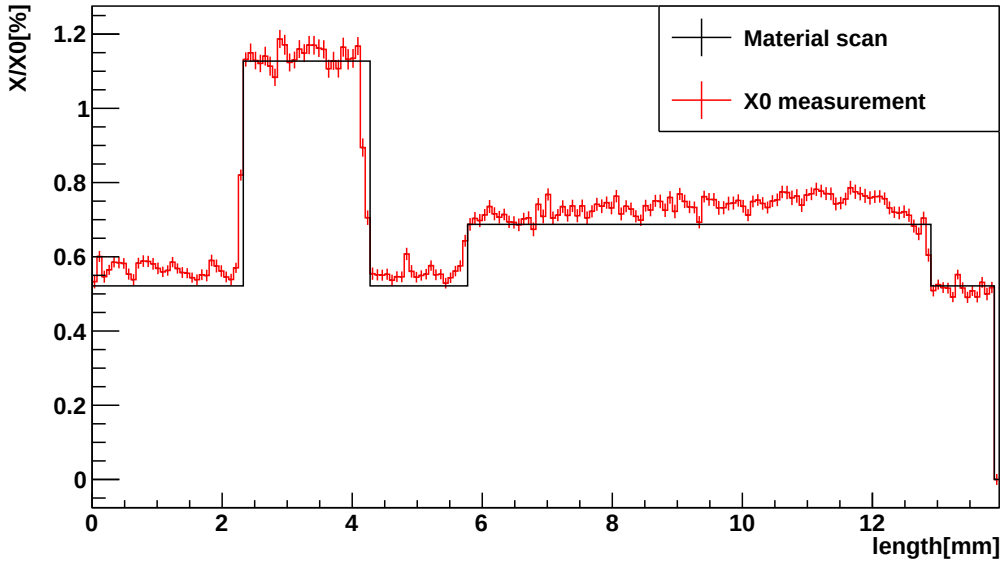

Figure 5.16 – A projection in the v-direction showing the differences in the material profile of the simulated and measured SVD ladders after improvements.

6

Review of Material Budget in Basf2

In this section, the amount of material in all the sub-detectors of the Belle II simulation is studied and documented. This study is a follow up to the study conducted by B. Golob and M.Lubej as documented in Belle2-Note-022 [9]. The amount of material in release-06 (December 2015) is compared with the most recent release of the software, release-08 (January 2017); the differences found are highlighted and discussed. These versions of the software were chosen simply because their release coincided with the start and end of this thesis project.

6.1 Methodology

The material profiles shown here are generated using the Material Scan tool as was explained in Chapter 4. To derive more detailed results from the scans, a number of macros were used to create angular projections and 2D comparison plots; an explanation on how the interpret the 2D difference plots and the 1D angular projections can also be found in Chapter 4.

6.2 Global view of inner detectors

For the first part of this study, the overall material profile of the inner detectors is presented. This includes the interaction region (IR), PXD, SVD and the

CDC. The IR consists of the Magnetic Field, Beam Pipe, Cryostat and Heavy Metal Shield. It is important to accurately know the amount of material in the inner detector as it is extremely sensitive due to its proximity the interaction point. In addition, since it carries very little material, even the slightest change can cause an appreciable difference in the material budget.

The cumulative amount of material in the inner detector for release-06 and release-08 is shown in figure 6.1 and figure 6.2 respectively. These plots focus on the material content of the region in the center and the information at low and high θ is off the scale; this was done since those regions are outside the tracking acceptance and don't impact the physics as much as the center. The differences in material content between the two releases was compared using difference scans and no material was observed to be added for these detectors in the central region. This can also be seen in figure 6.3 which was generated by overlaying the two plots. While there were changes made between these releases, those appear outside of the region being explored in these plots and will be shown in more detail in the following sections.

The amount of material in the central region is also compared with the results from [9] and summarized in table 6.1. There is a slight increase in the material of 0.002 X_0 in the interaction region and also in the PXD compared to the previous study as indicated.

	Material in this study $[X/X_0]$	Material in previous study$[X/X_0]$ [9]
IR	0.01	0.008
IR+PXD	0.0125	0.01
IR+PXD+SVD	0.045	0.045
IR+PXD+SVD+CDC	0.07	0.07

Table 6.1 – Comparison of inner detector material between this study and the previous one in [9].

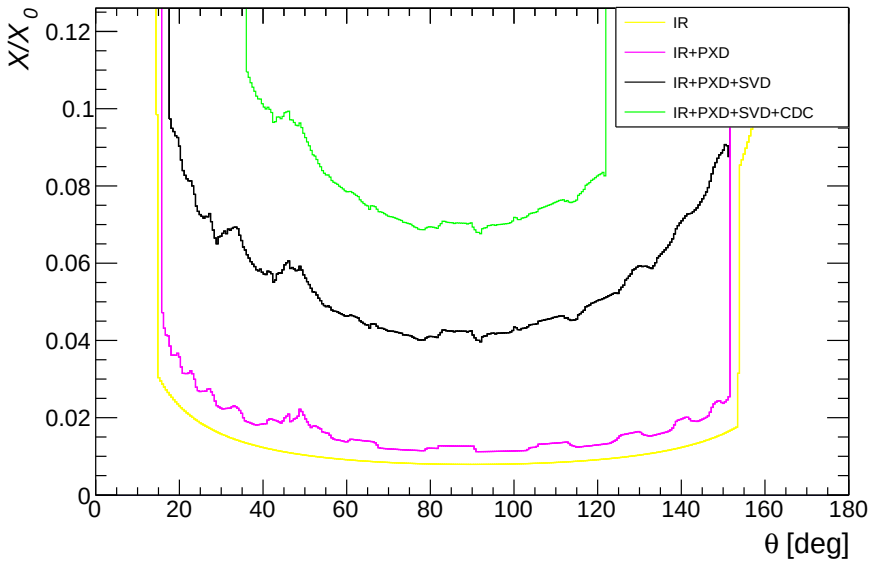

Figure 6.1 – Global view of inner detectors from release-06. This plot represents the number of radiation lengths of material (X_0), averaged over ϕ, that a particle from the origin would traverse if traveling at an angle θ. The colors represent the various subsystems, and the plots are cumulative, for e.g the green curve represents amount of material not only in the CDC, but also that of subsystems in front of it.

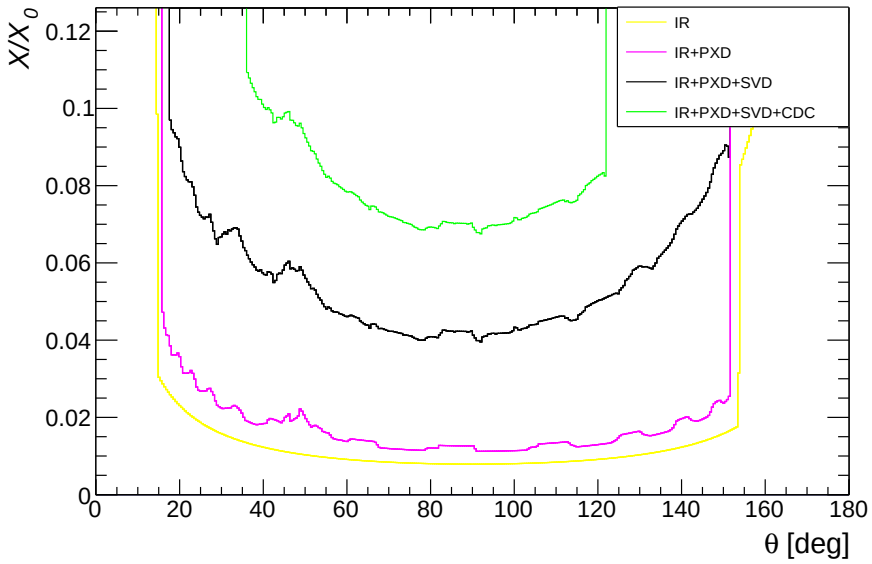

Figure 6.2 – Global view of inner detectors release-08. This plot represents the same information as the previous one but for the new release.

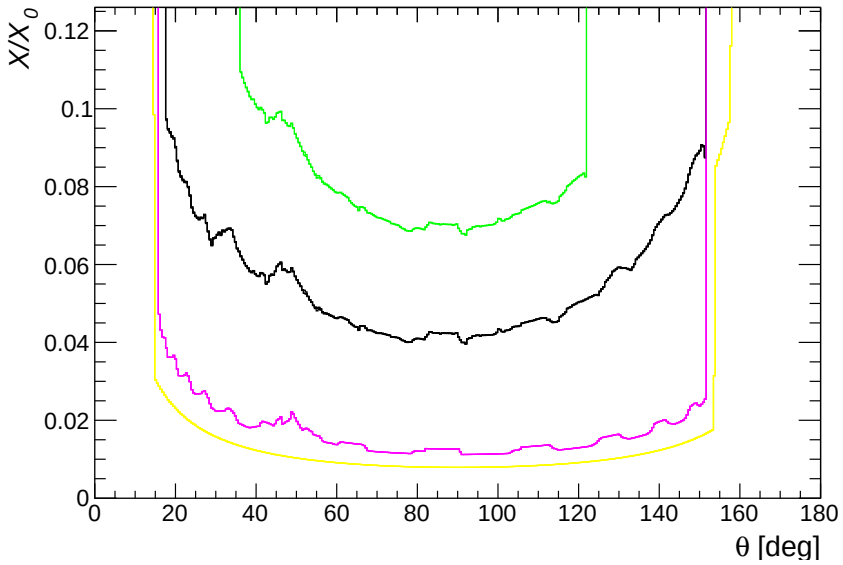

Figure 6.3 – Comparison of inner detectors between release-06 and release-08 by imposing figure 6.1 on top of figure 6.2. No deviation between the overlapping curves indicates the material content remained the same in the central region between the releases.

6.3 PXD

The amount of material in the PXD supports and the central region in release-06 is indicated in figures 6.4 and 6.5 respectively. It averages at 1.6 X_0 and 1.0 X_0 in the forward and backward supports respectively. In the central region, which lies within the acceptance region, it averages at 0.01 X_0. The groove structure of the PXD ladders is evident in the alternating peaks and troughs observed in the angular projection plot.

In figures 6.6 and figure 6.7 the amount of material between releases-06 and release-08 is compared. As is evident, there were no changes in the support structure or the central region. Note that the improvements to the PXD ladders which were shown in chapter 5 were not a part of release-06 or release-08 and still have to be committed to the master branch of basf2; those changes thus don't appear here.

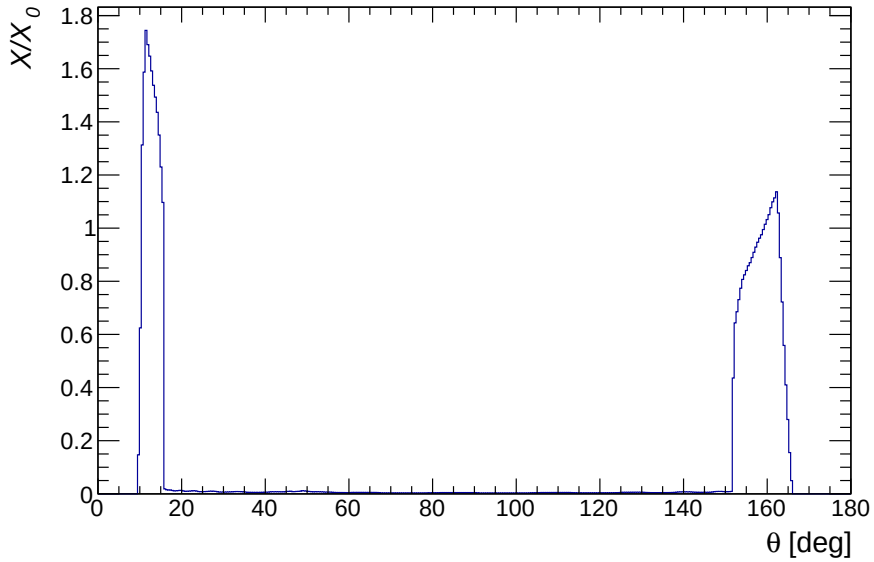

Figure 6.4 – Material in the PXD supports as seen in release-06. This plot represents the number of radiation lengths of material, averaged over phi, that a particle from the origin would traverse if traveling at an angle θ.

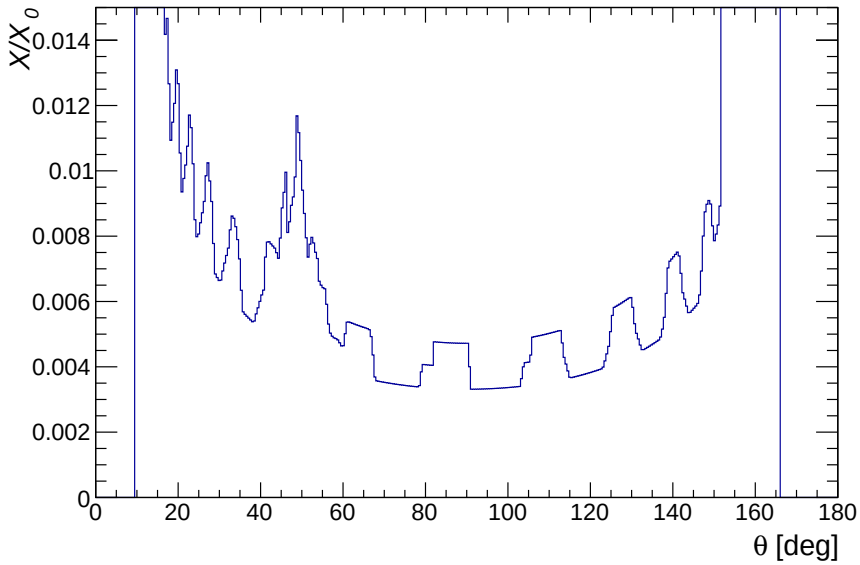

Figure 6.5 – Material in the PXD central region as seen in release-06. The peaks and troughs observed are a result of the grooves in the PXD ladders.

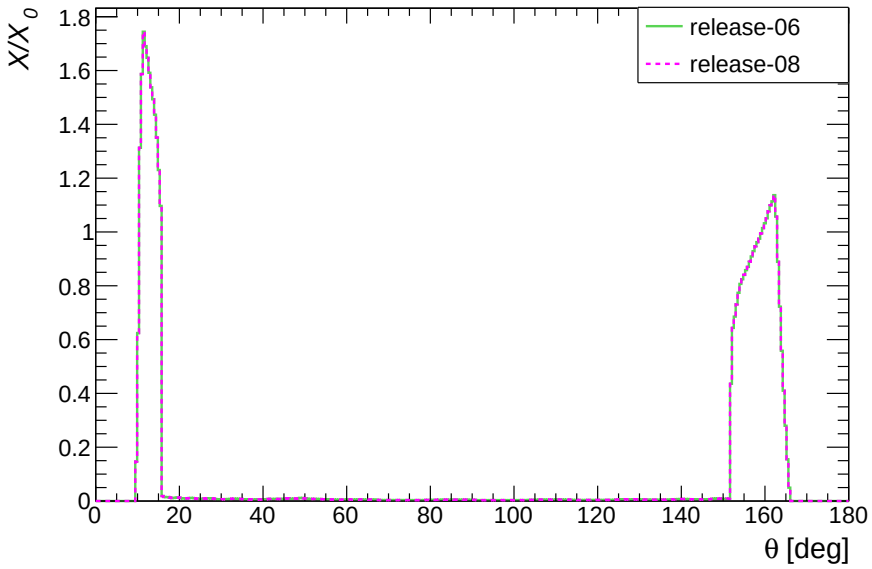

Figure 6.6 – Comparison of material in PXD supports between release-06 and release-08. No difference is observed in the material profile between the two releases.

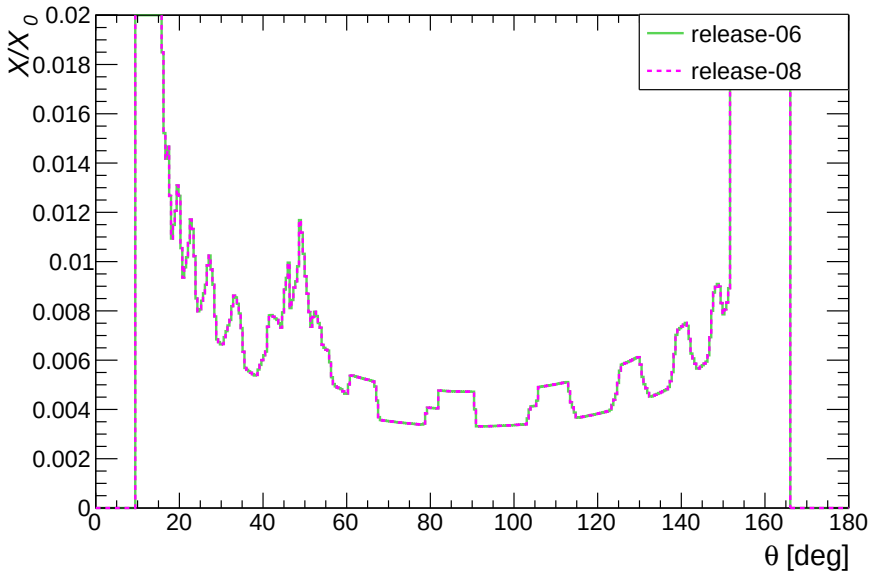

Figure 6.7 – Comparison of material in PXD central region between release-06 and release-08. No difference is observed in the material profile between the two releases.

6.4 SVD

The amount of material in the SVD supports and the central region is indicated in figure 6.8 and figure 6.9 respectively. It averages at 3.5 X_0 and 3.0 X_0 in the forward and backward supports respectively. In the central region, which lies within the fiducial acceptance, the material budget averages at 0.04 X_0. In figure 6.10 and figure 6.11 releases 6 and 8 are compared. There were no changes observed in the support structure or the central region. Similar to the case of the PXD, the improvements to the SVD ladders which were shown in chapter 5 are not a part of release-06 or release-08; those changes thus don't appear here.

In figure 6.12 and figure 6.13 planar scans of the SVD in the xz and xy planes are shown. These indicate the finer details of the differences in the material profile of the SVD ladders and supports; they also highlight the geometry of the ladders.

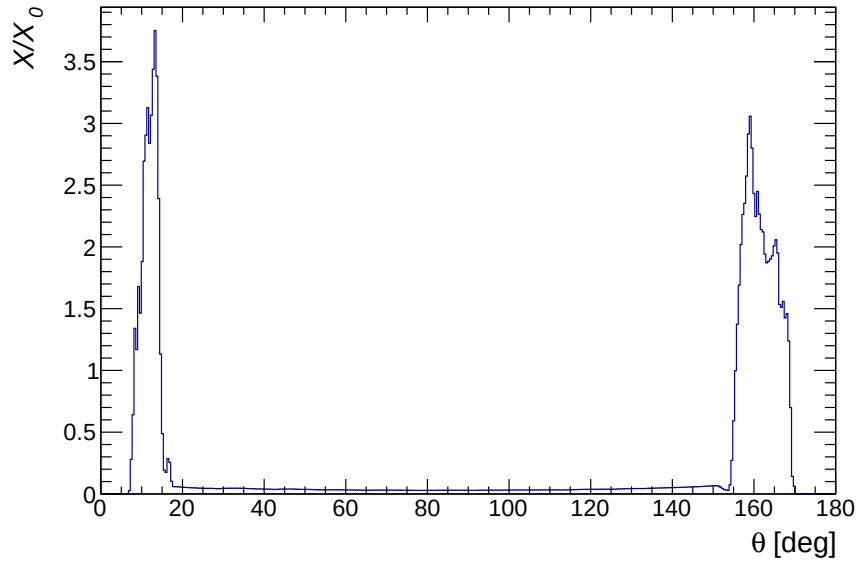

Figure 6.8 – Material in the SVD supports as seen in release-06.

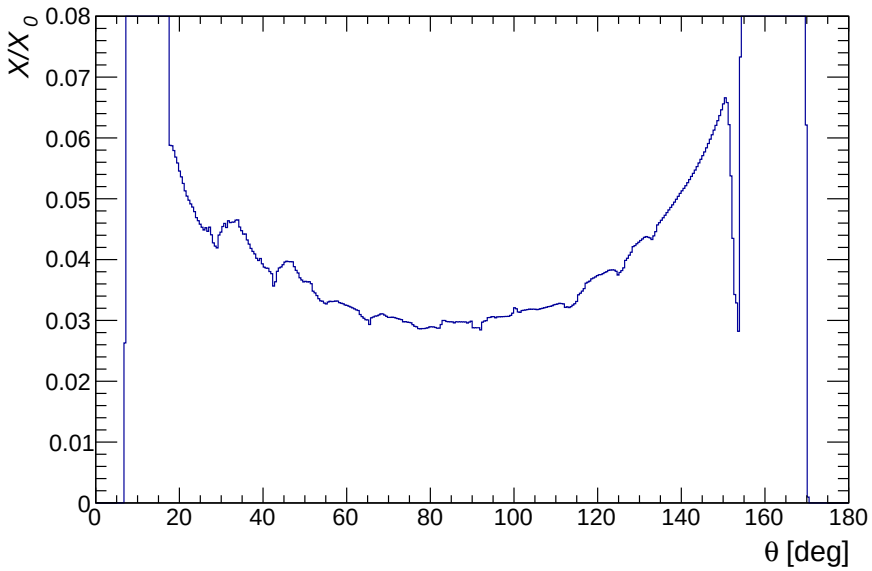

Figure 6.9 – Material in the SVD central region as seen in release-06.

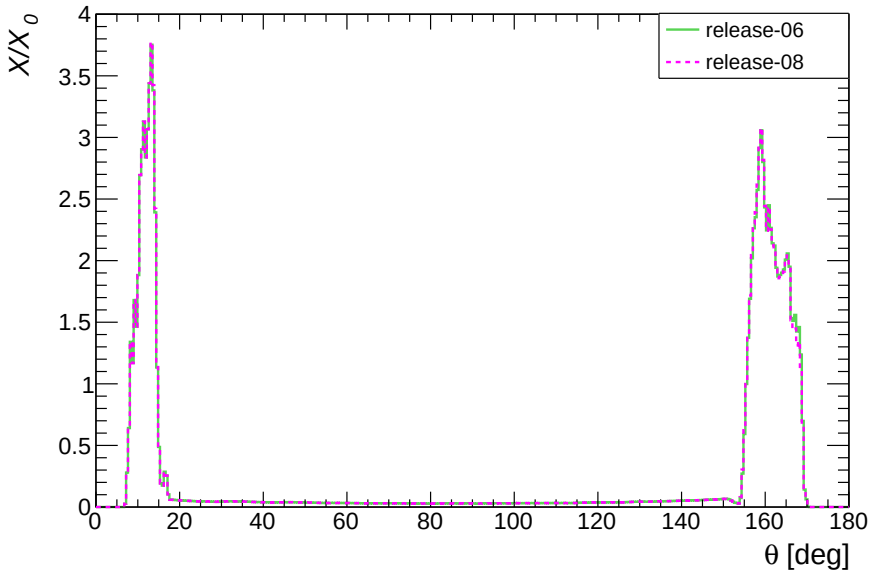

Figure 6.10 – Comparison of material in the SVD supports between release-06 and release-08. No difference is observed in the material profile between the two releases.

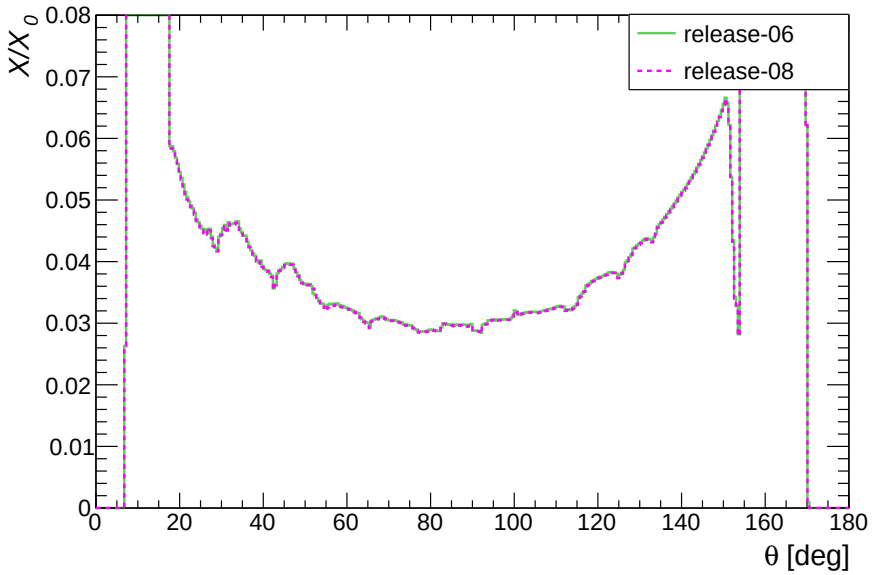

Figure 6.11 – Comparison of material in the SVD central region between release-06 and release-08. No difference is observed in the material profile between the two releases.

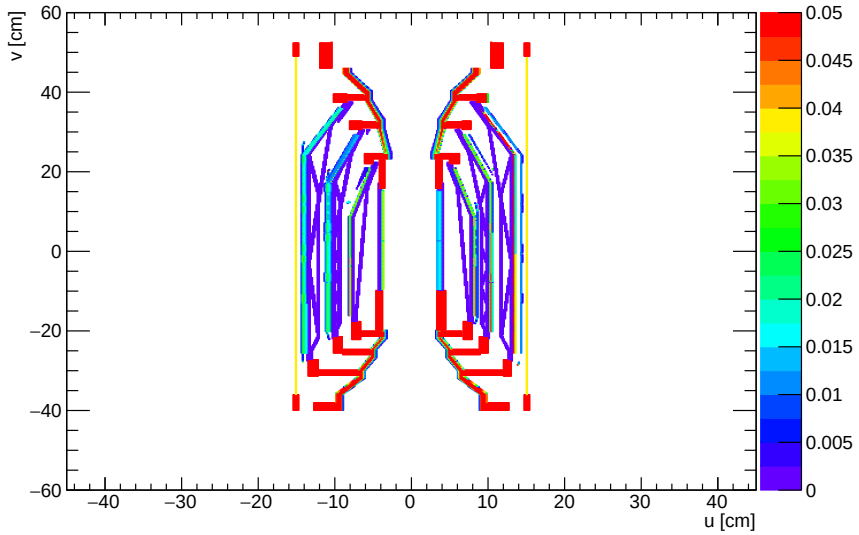

Figure 6.12 – Planar Scan of the SVD material profile in the xz plane. The coloured legend on the right indicates the amount of material in X_0. Finer details of the geometry of the four SVD ladders can be seen.

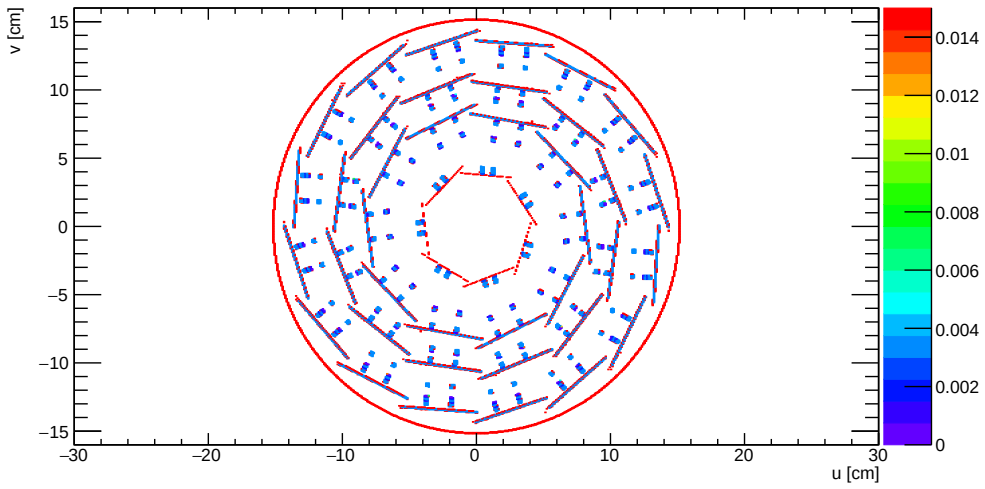

Figure 6.13 – Planar Scan of the SVD material profile in the xy plane. The cylindrical layout of the SVD is evident which provides for 360° coverage in ϕ.

6.5 CDC

The material profile in the CDC supports and the central region can be seen in figure 6.14 and figure 6.15 respectively. It averages at 8.5 X_0 in the front end and 3.5 X_0 in the backward support.

In the central region, which lies within the fiducial acceptance, the material profile is more complicated. In the forward end, the budget averages at 0.15 X_0 which is the same as documented in the previous study [9]. However, in the back-end, the material on average is 0.45 X_0 which is an increase from the 0.35 X_0 as found in [9]. The profile in the backward support between 120° and 160° is a result of the structure of the rings behind the end plates as indicated in figure 6.19.

In figures 6.16, 6.17 and 6.18 releases 6 and 8 are compared. Figure 6.16 is a difference plot indicating the profile and location of the changes by taking the difference between two spherical material scans; figures 6.17 and 6.18 are angular projections averaged over the ϕ direction. There appears to be a difference of about 2 X_0 of material in the supports while material in the central region appears shifted.

The main source of these changes is a shift in the forward and backward endplates in the z-direction. These changes were made to bring the CDC implementation in the simulation closer to the actual geometry. The front endplate is divided into three parts: small, canonical and main; the shift in all three parts along with the backward endplate is summarized in table 6.2. This shift has resulted in the acceptance region increasing by about 30 mm. The addition of material in the supports is a result of finer adjustments to the material in the cover, rings and board mounts which are shown in figure 6.19

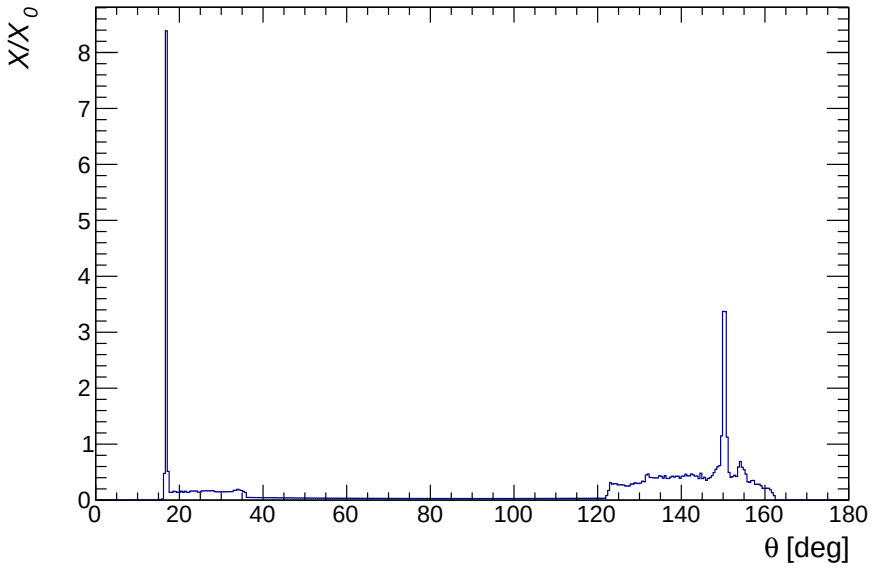

Figure 6.14 – Overall material in the CDC as seen in release-06.

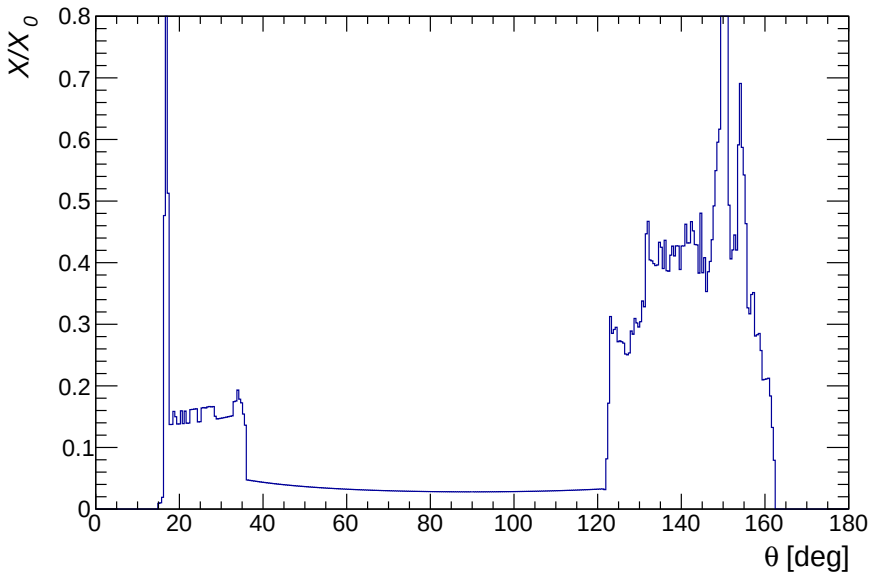

Figure 6.15 – Material in the CDC central region as seen in release-06.

	Shift in Forward Endcap [mm]
Small Canonical Main	+22.6 +20.5 +17.5
	Shift in Backward Endcap [mm]
	-12.5
	Change in sensitive region [mm]
	+30

Table 6.2 – Changes made to the position of the CDC endcaps in the z-direction for release-08.

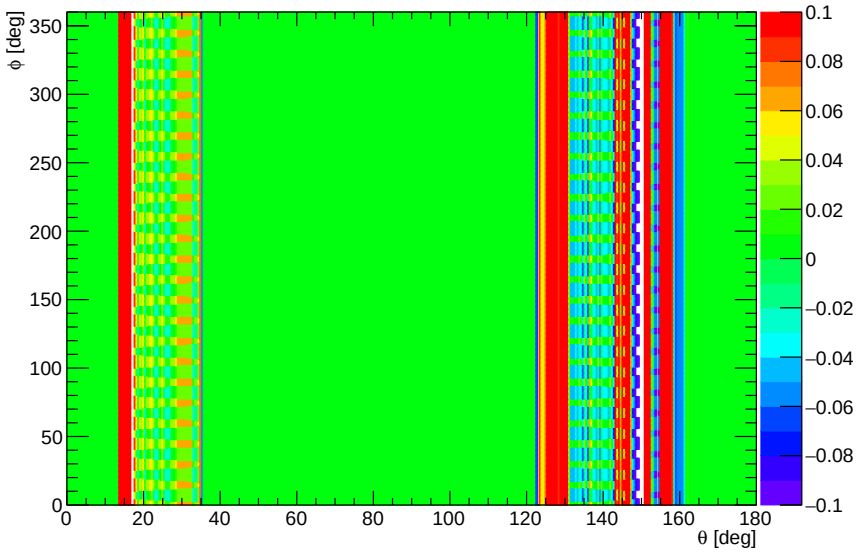

Figure 6.16 – Comparison of material in release-06 and release-08 of the CDC; the scale on the right indicates the amount of material in X_0. The plot was generated by taking the difference between two spherical scans in the different releases. Addition of material is indicated by positive X_0 and a decrease is shown by negative values.The change observed arises due to the shift in the forward and backward endplates in the z-direction.

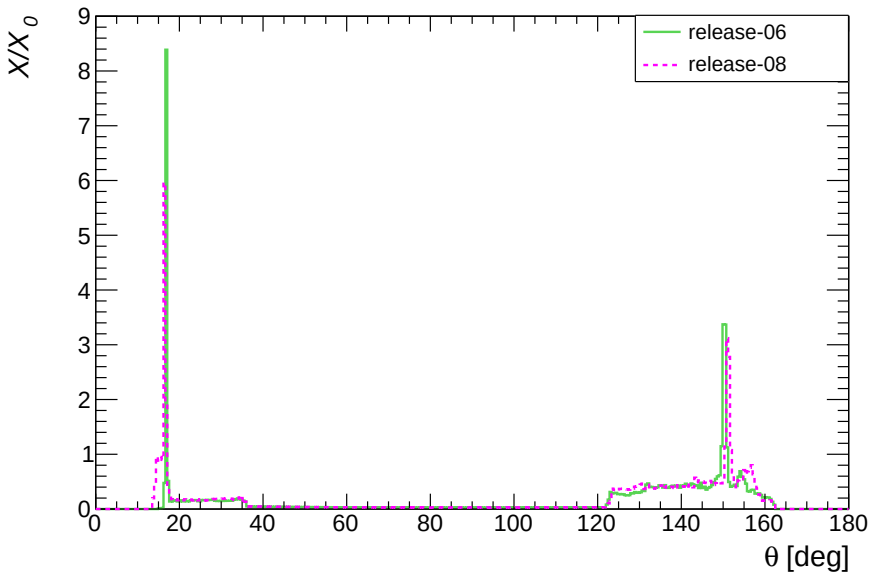

Figure 6.17 – Comparison of material in the CDC between release-06 and release-08

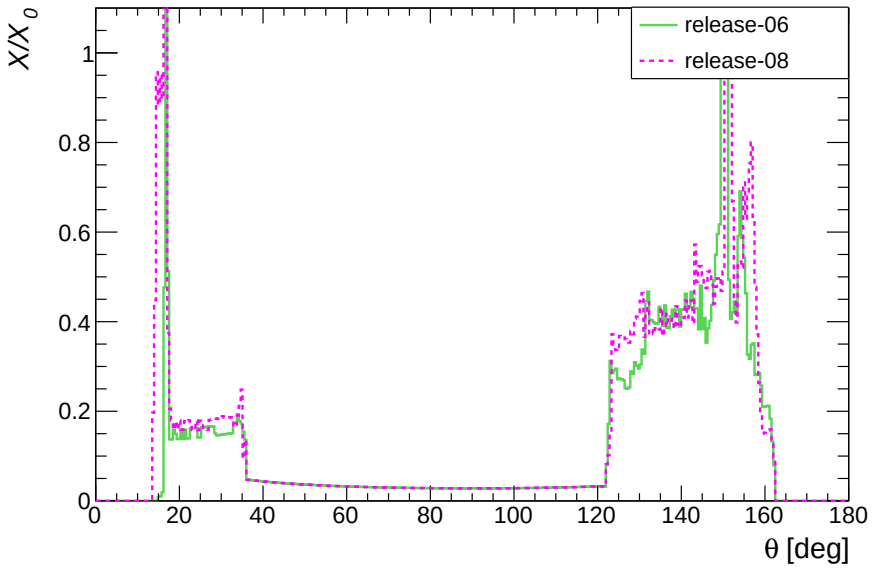

Figure 6.18 – Comparison of material in CDC between release-06 and release-08. The discrepancy seen arises due to the shift in the forward and backward endplates in the z-direction as outlined in table 6.2.

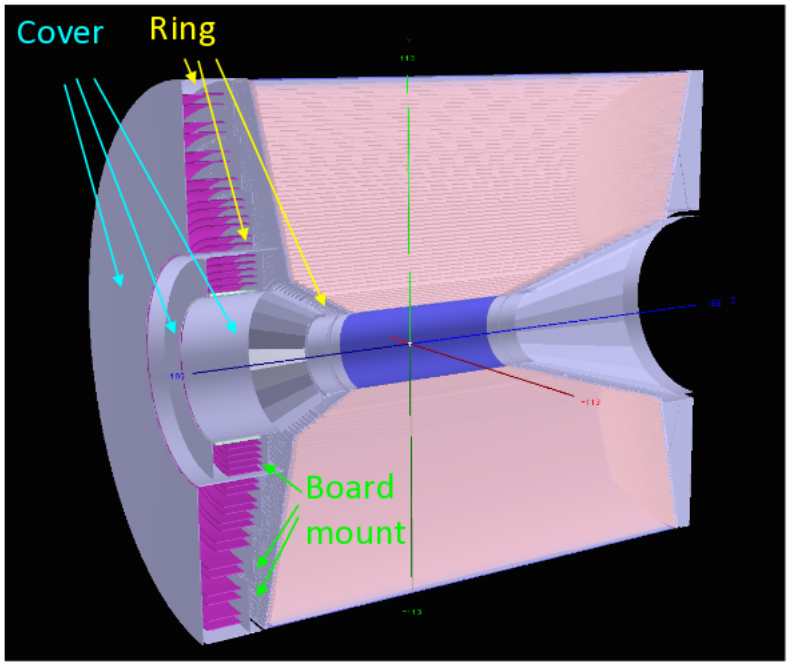

Figure 6.19 – A schematic showing the inner structure of the CDC. The cover, rings and board mounts in the endcaps are indicated which are responsible for the uneven profile seen in figure 6.15 between 120° and 160° [28].

6.6 TOP/COIL

The material profile in the TOP and solenoid COIL structures for release-06 can be seen in figures 6.20 and 6.21 respectively. The amount of material, averaged over ϕ, is 0.17 X_0 and 2.25 X_0 at θ of 90° for the TOP and COIL respectively. The previous study [9] found the TOP material to be 0.20 X_0 so there has been a decrease in the material simulation since that release.

It is important to understand the profile of the material in this particular case. The gradient in the profile from the front to the back, corresponding to a decrease from 0.3 X_0 to 0.16 X_0, represents the different amount of material the geantinos 'see'. As can be seen in the graphical implementation in figure 6.22 and 6.23, both structures are symmetrical and have uniform physical thickness. The gradient observed is due to the geantinos in the Material Scan simulation traversing a longer length of the material when they do not pass the structure perpendicularly. Thus, the actual material in the central region of the TOP module is represented at the 90° point. As for the peak which is observed at the very end, this is due to boards, PMTs and cooling pipes present in the structure at the end of the modules as indicated in figure 6.24. These rest outside the acceptance region, so do not impact the physics directly.

In figures 6.25, 6.26 and 6.27 material profiles for releases 6 and 8 are compared. Figure 6.25 is a spherical difference plot indicating the profile and location of the changes while figures 6.26 and 6.27 are angular projections averaged over the ϕ direction. In the case of the COIL, no differences are observed. However, there is a small difference of 0.01 X_0 for the TOP. No new material was added between these releases and the only difference in the geometry is due to a rotation

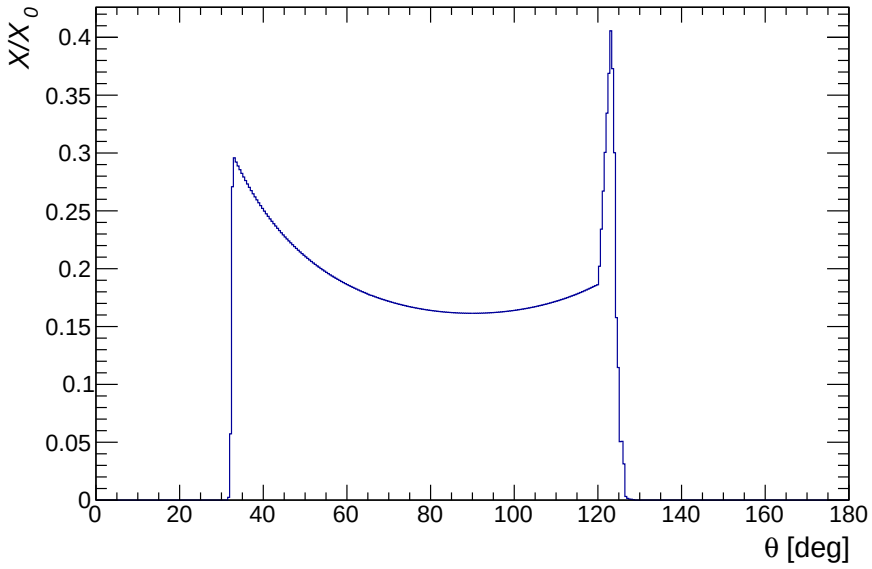

Figure 6.20 – Overall material in the TOP as seen in release-06.

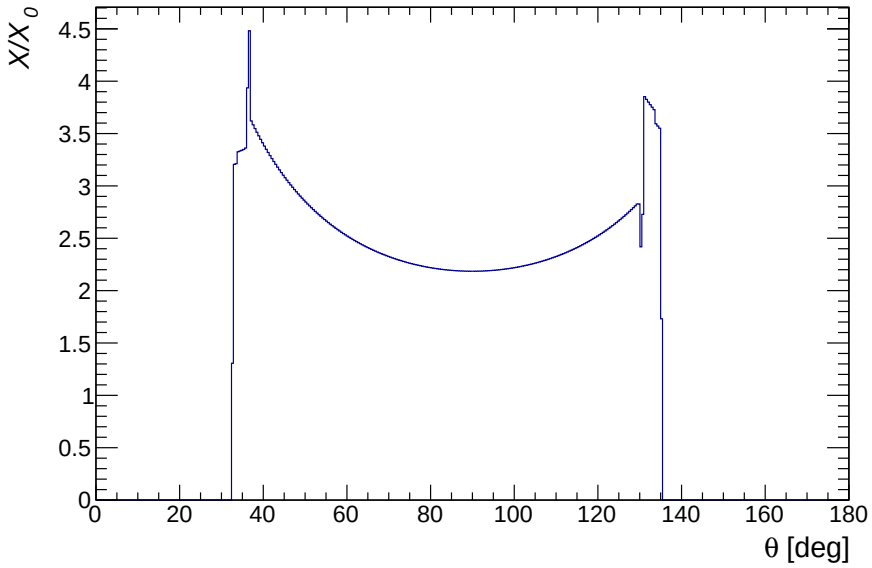

Figure 6.21 – Overall material in the COIL as seen in release-06.

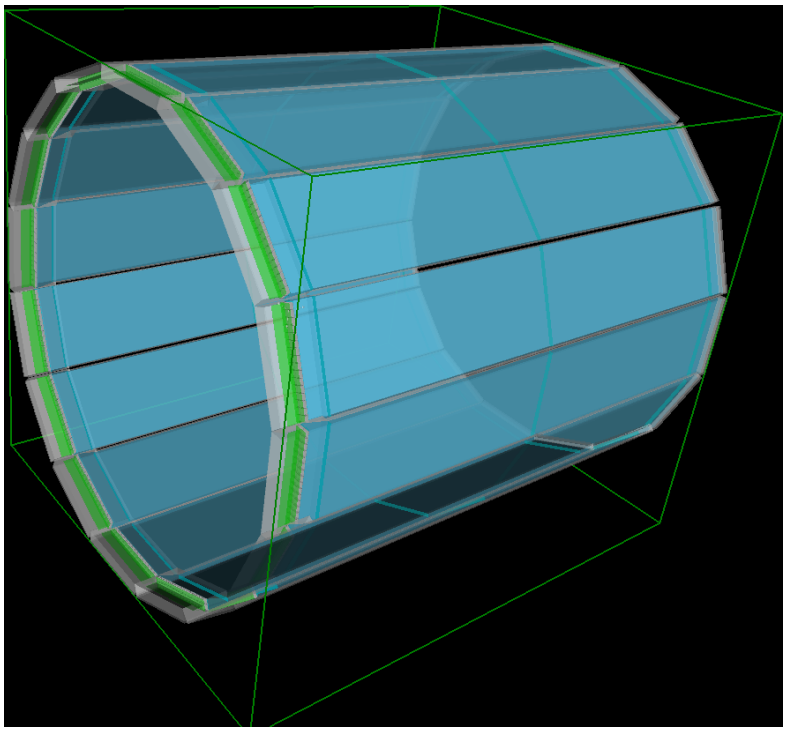

Figure 6.22 – Geometry of the TOP modules organized in a cylinder configuration in basf2.

in ϕ of half the module width. This is in agreement with the difference scan in figure 6.25 which indicates an addition of about 0.2 X_0 (indicated by the yellow lines) and a reduction of 0.2 X_0 (indicated by the blue lines) near the perimeter of the rectangular modules. The net change in material should thus be almost zero; which is in agreement with the small change of 0.01 X_0 seen in projection plot in figure 6.26.

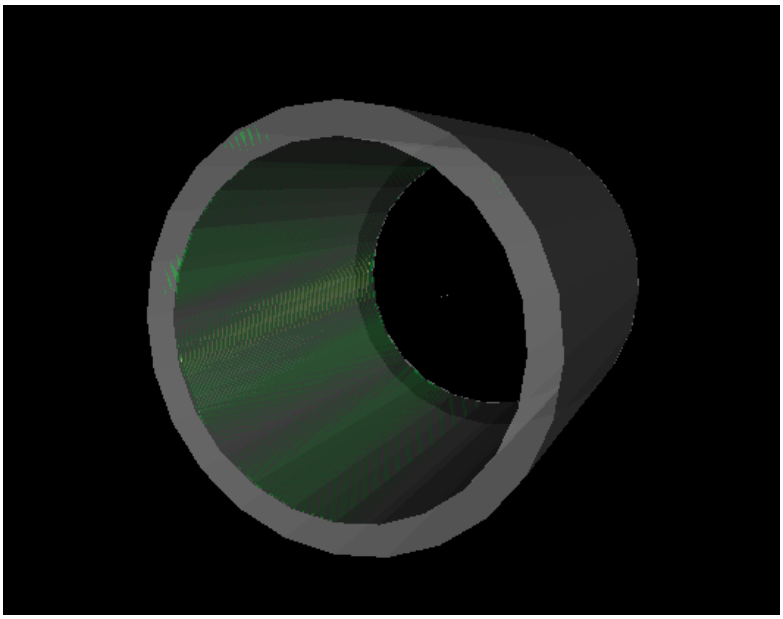

Figure 6.23 – A visualization of the geometry of the COIL in basf2.

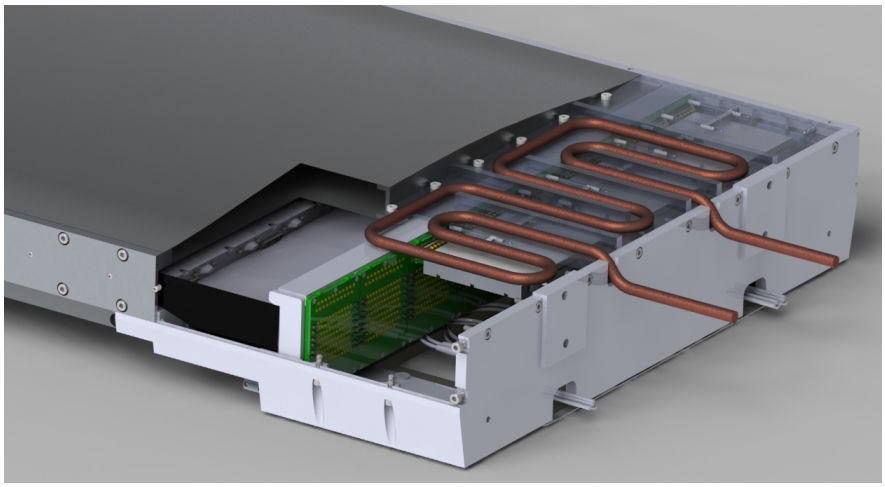

Figure 6.24 – Support structure in at the end of the top module responsible for the peak seen in figure 6.20.

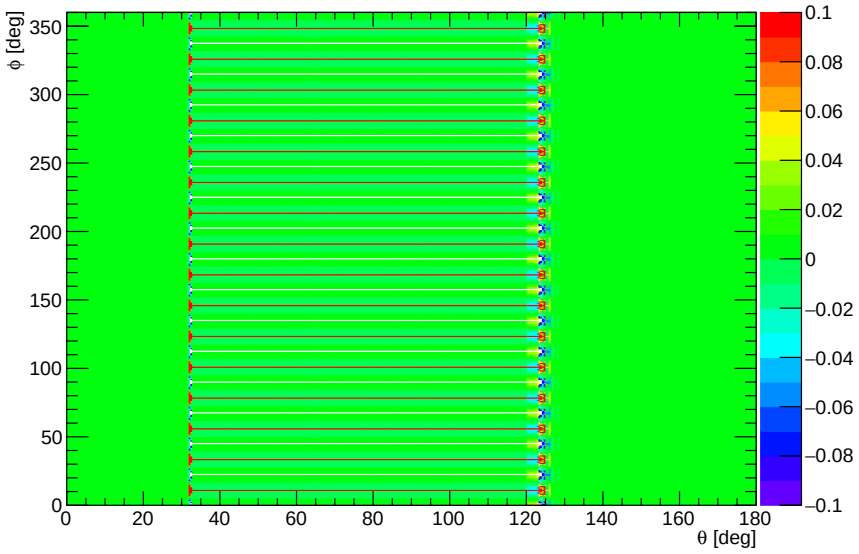

Figure 6.25 – Comparison of material in TOP between release-06 and release-08; plot highlights the change in material between releases. The scale on the right indicates the amount of material in X_0; the plot was generated by taking a difference between two spherical scans. Positive X_0 corresponds to an increase in material and negative to a decrease. The plots indicate an addition of about 0.2 X_0 (indicated by the yellow lines) and a reduction of 0.2 X_0 (indicated by the blue lines).

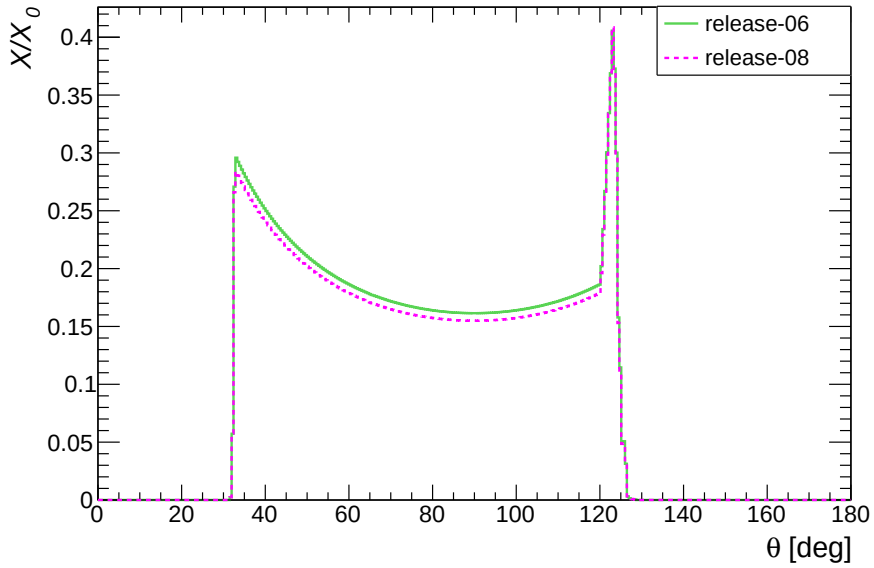

Figure 6.26 – Comparison of material in TOP between release-06 and release-08. In this release, there was rotation in ϕ of half the module width which is appearing as a small increase in material.

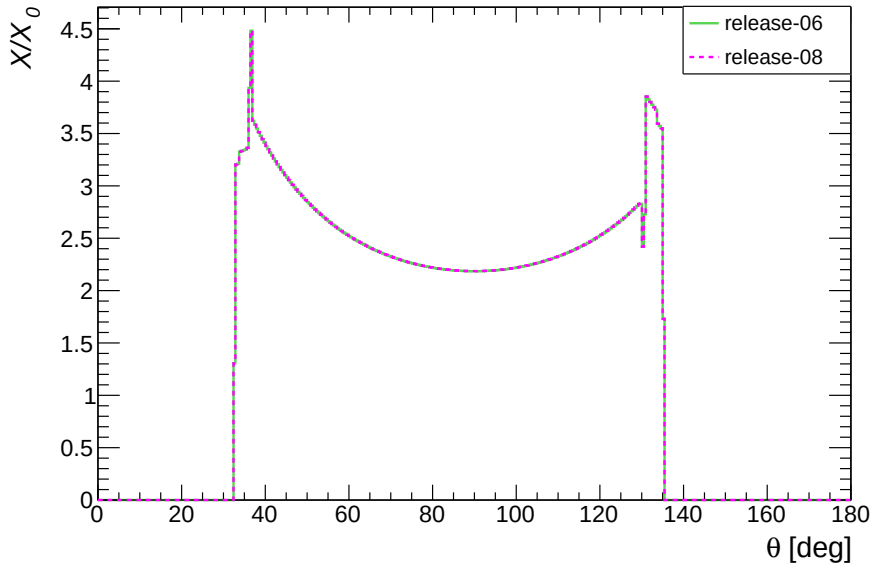

Figure 6.27 – Comparison of material in COIL between release-06 and release-08. No changes are observed.

6.7 ARICH

The material profile for the ARICH is shown in figure 6.28. It averages at 0.26 X_0 in the sensitive region which is consistent with the results found in [9].

In figure 6.30 releases 6 and 8 are compared. Figure 6.29 is a difference plot for the two different releases indicating the profile and location of the changes. The amount of material appears to have doubled in ARICH. There were a number of changes that were made to the geometry which account for the changes observed; these are summarized as follows:

- thickness of aluminum support plate for aerogel plane was changed from 2 mm to 1 mm.
- geometry of aluminum support plate of the photon detectors plane was updated. The thickness of the support plates was updated from 4mm to 2mm. In addition, backwalls were added between the photo-detector slots. This change is the biggest contributor to the increase in the material and explains the peak at about 18° in figure 6.30.
- an aluminum support structure cylinder was added on the inner side of the ARICH. The cylinder is 1.5 cm thick and 30 cm long and explains the increase in material in the central region; it can be see in figure 6.31.
- a similar aluminum support structure added on the outside of the ARICH. The cylinder is 1 cm thick and 30 cm long and accounts for the increase in material in the central region as well.

Figure 6.31 provides visual comparison of the changes between the releases which have been summarized above.

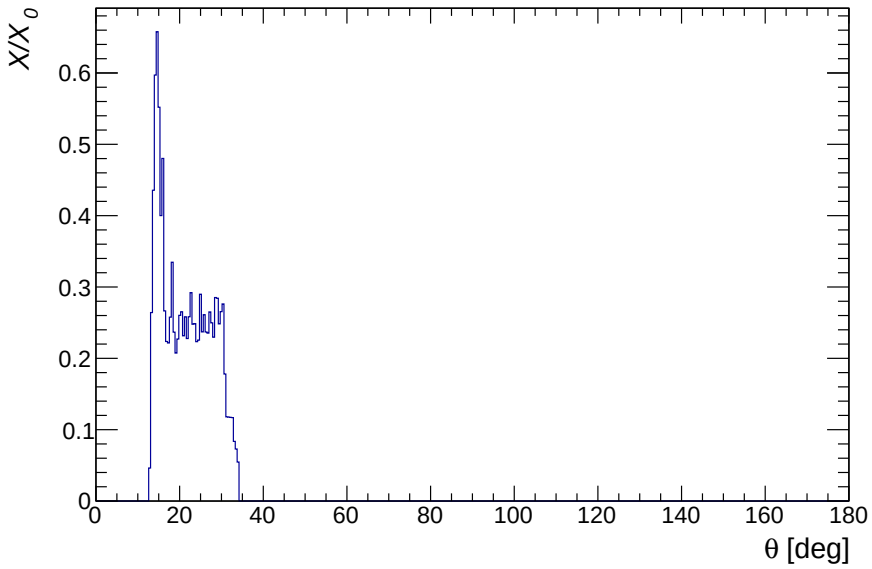

Figure 6.28 – Overall material in the ARICH as seen in release-06.

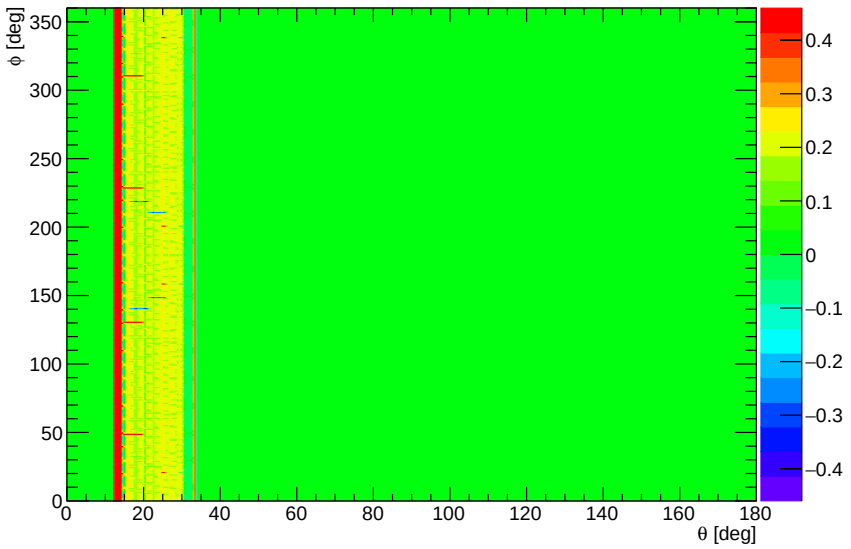

Figure 6.29 – Comparison of material in ARICH; plot highlights the amount and location of material changed between releases. Positive X_0 corresponds to an increase in material and negative to a decrease.

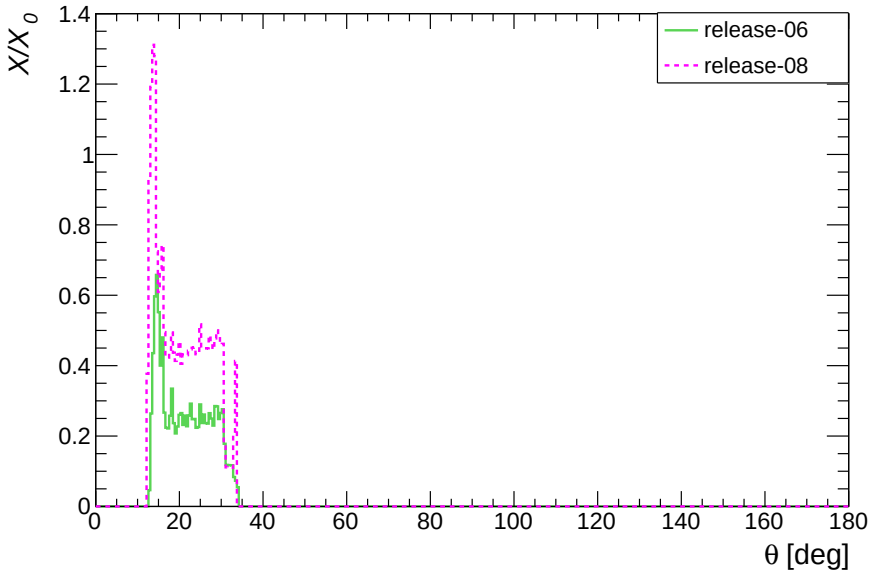

Figure 6.30 – Comparison of material in ARICH between release-06 and release-08. Increase in the material in the new release is due to addition of the cylindrical supports and addition of aluminum backwalls.

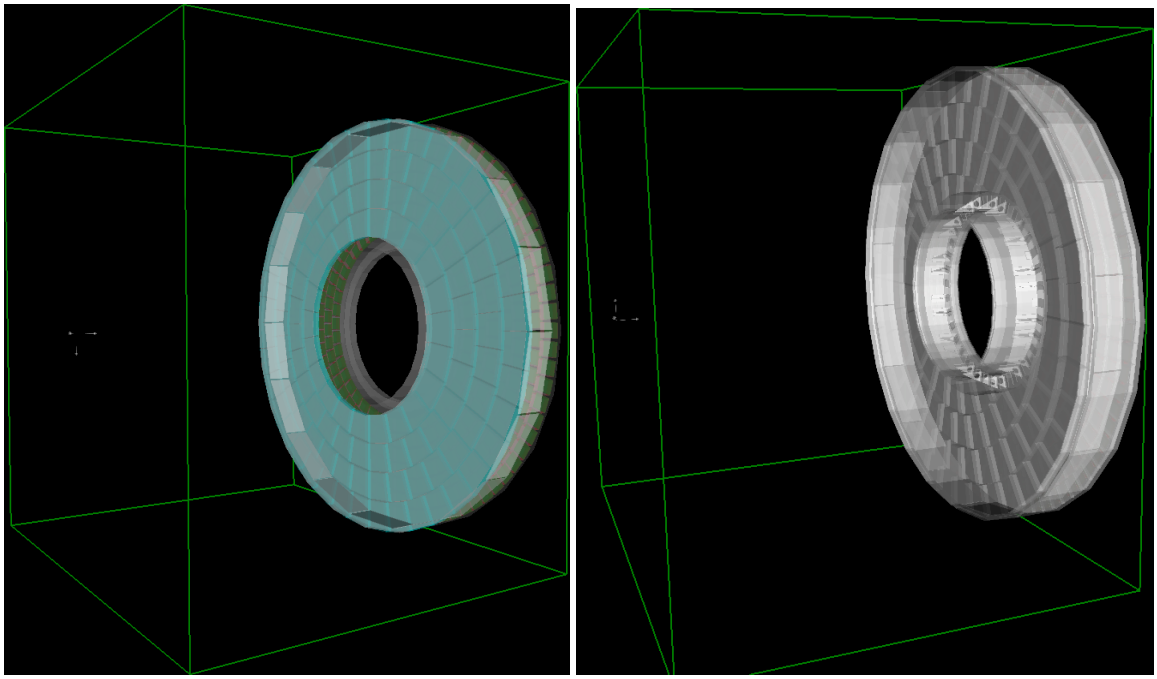

Figure 6.31 – A visual comparison of the ARICH between release-06 (left) and release-08 (right). The addition of the cylindrical aluminum supports on the inner and outer edges can be seen; the change in thickness of the support plate covering the face of the detector is also noticeable.

6.8 ECL

A spherical and planar material scan indicating the material profile of the ECL is shown in figure 6.32 and figure 6.33; an angular projection of the spherical scan is shown in figure 6.34. The material in the barrel region averages at about 19 X_0 while it peaks at 28 X_0 in the supports.

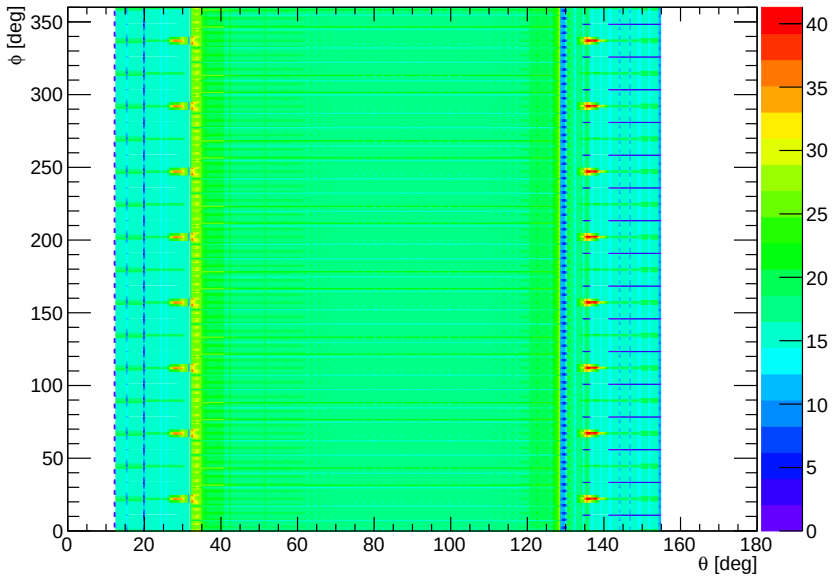

Figure 6.32 – A spherical material scan of the ECL showing the material profile in the barrel region from release-06.

The differences found in the material profile between release-08 and release-06 are depicted in figures 6.35 and 6.36. As can been seen, a reduction of material by 1 X_0 is observed in the barrel region and the end cap supports show an increase in the material.

There were a number of changes made to the ECL in release-8 which can account for these changes. Foremost is the implementation of a new geometry with corrected crystal shapes of the calorimeter based on engineering drawings.

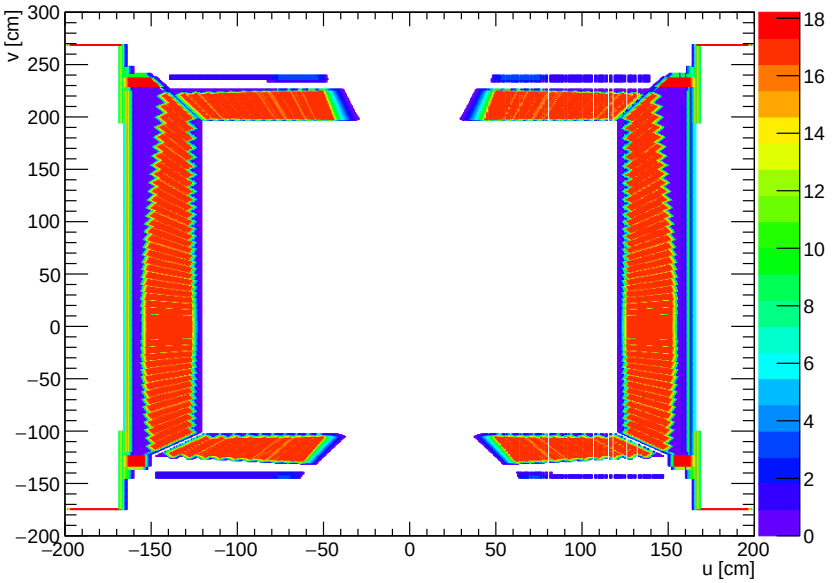

Figure 6.33 – A planar material scan of the ECL showing the material profile in the xz plane in release-06.

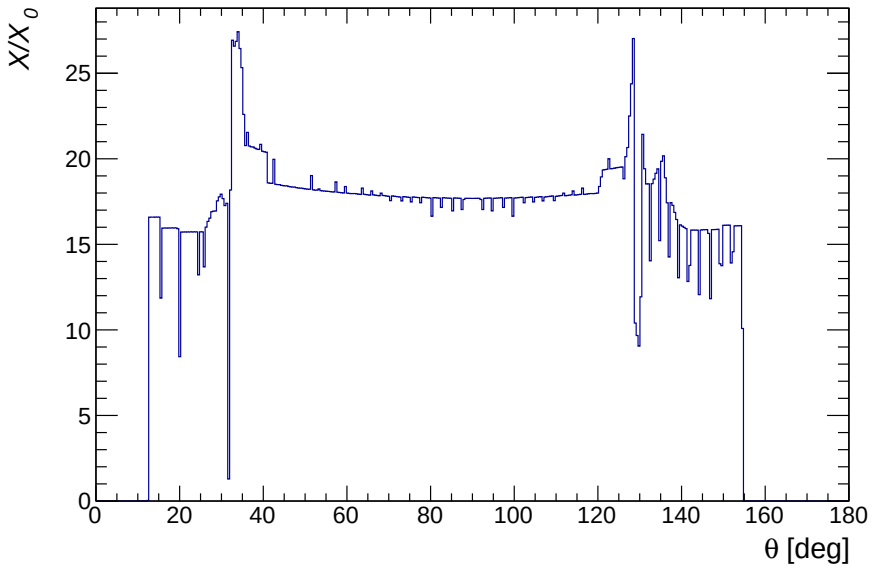

Figure 6.34 – Overall material in the ECL in the barrel and endcap region as seen in release-06. The barrel region lies approximately between 30° and 130°.

Figure 6.37 provides visual comparison of the changes between the releases. The summary of the changes is itemized below:

- in the barrel region, the steel sheet in front of the crystals was changed to aluminum; this is the prime contributor to the reduced material budget in this area.
- addition of 1.5 mm aluminum sheet infront of the crystal in the endaps which explains the general material increase in this region.
- addition of 20 mm stainless steel supporting rings in the endcaps.
- improvements to the endcap supporting structure shape based on engineering drawings.
- addition of at least 400 μm distance between all the crystals.

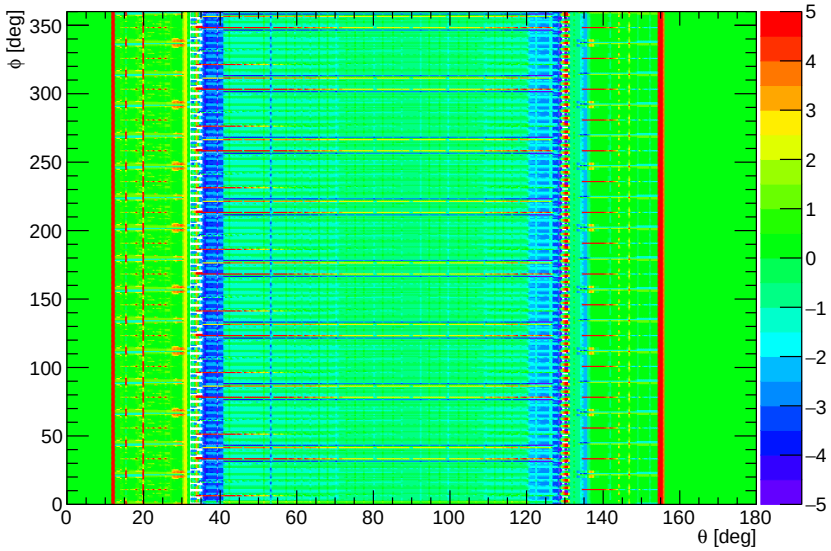

Figure 6.35 – Comparison of material in the ECL; plot highlights the amount and location of material changed between releases. The plot was generated by taking a difference in spherical material scans between release-06 and release-08. Positive X_0 corresponds to an increase in material and negative to a decrease.

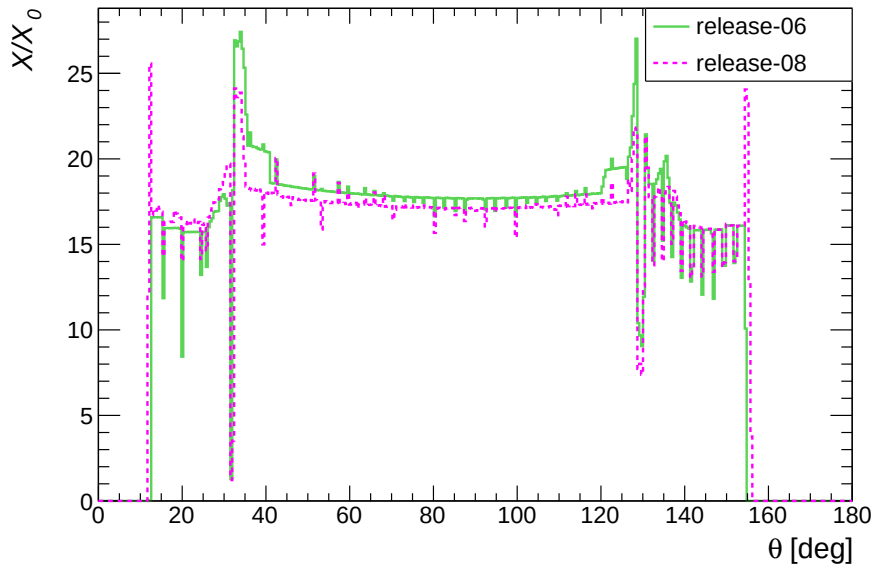

Figure 6.36 – Comparison of material in the ECL between release-06 and release-08. The difference in the barrel region is due to the the changes in crystal geometry and change of steel plates to aluminum. The discrepancy in the endcaps is due to the modifications to the support structure as shown visually in figure 6.37.

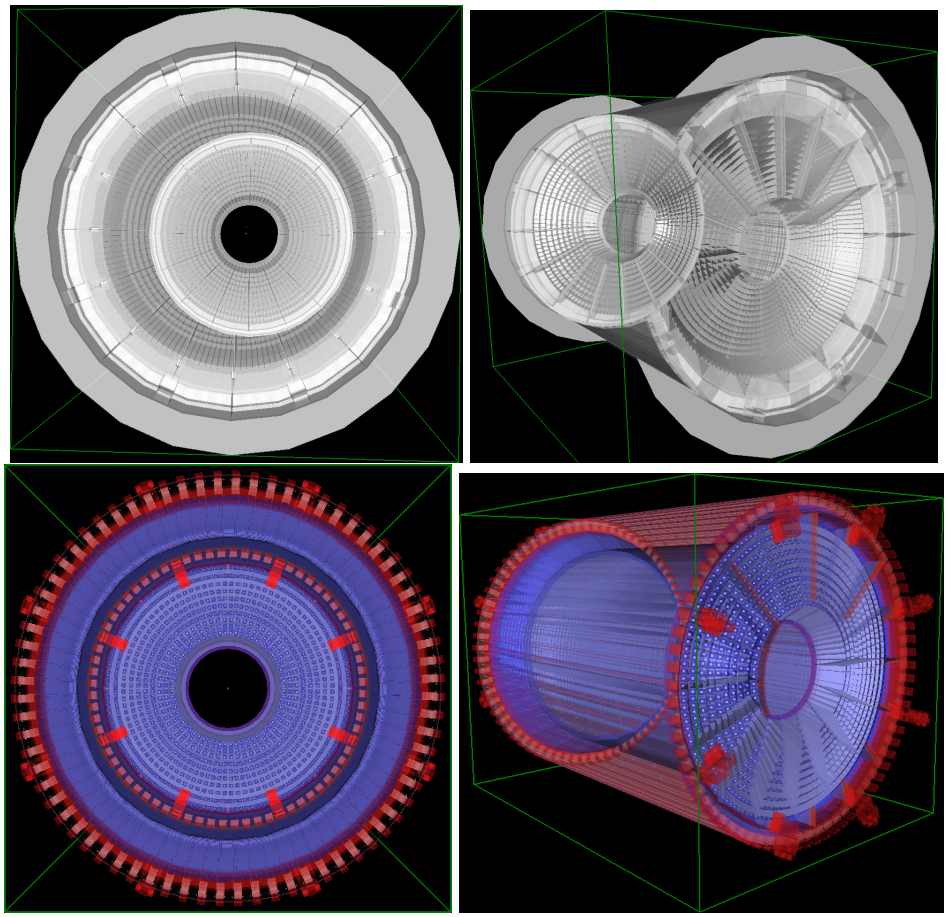

Figure 6.37 – A visual comparison of the ECL between release-06 (top) and release-08 (bottom). The images of the endcaps on the top and bottom left show the improvements to the support structure by the addition of stainless steel support rings; the change in crystal shapes and addition of spacing between them can also be seen. The top and bottom right images show the overall change in the barrel region due to the new crystal geometry. Improvements to the support structure are also visible.

6.9 EKLM/BKLM

The material profile in the EKLM and BKLM structures can be seen in figures 6.38 and 6.39 respectively. The BKLM has 54 X_0 of material in the central region while the EKLM peaks at about 70 X_0. The material profile between release 6 and 8 is compared in figure 6.40 and figure 6.41 and no differences are observed.

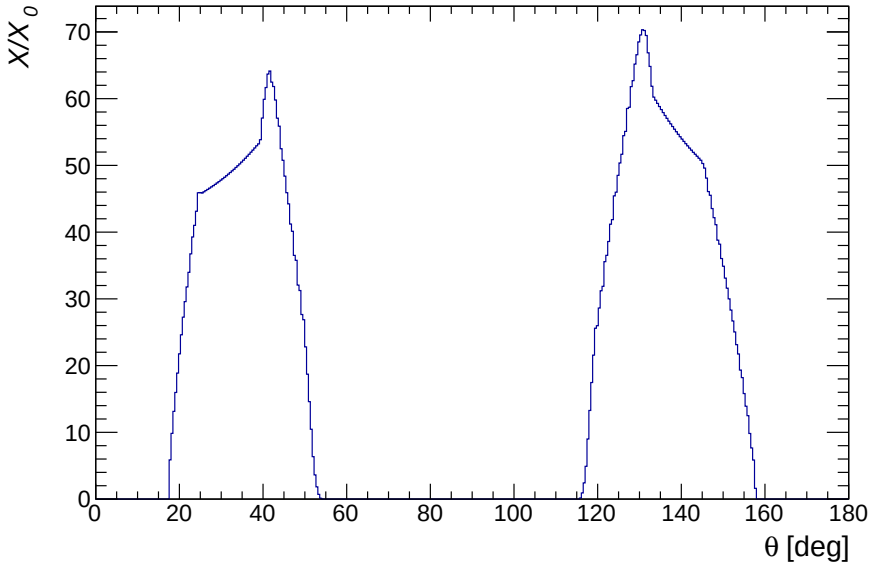

Figure 6.38 – Overall material in the EKLM as found in release-06.

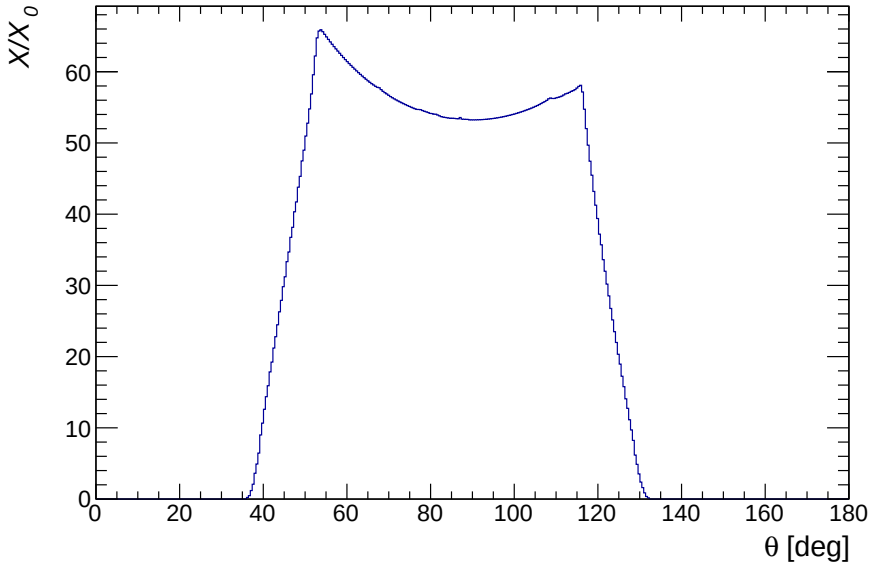

Figure 6.39 – Overall material in the BKLM as found in release-06.

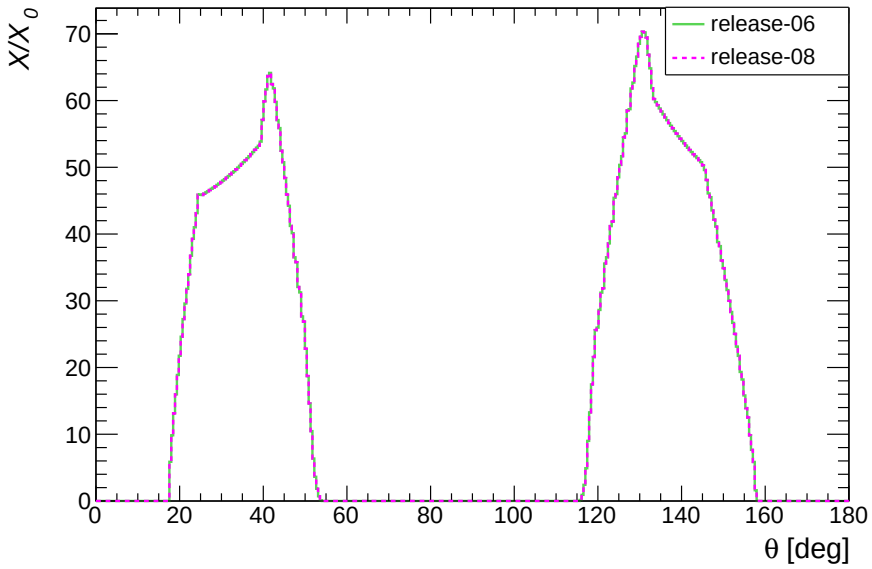

Figure 6.40 – Comparison of material in EKLM between release-06 and release-08. No changes are observed.

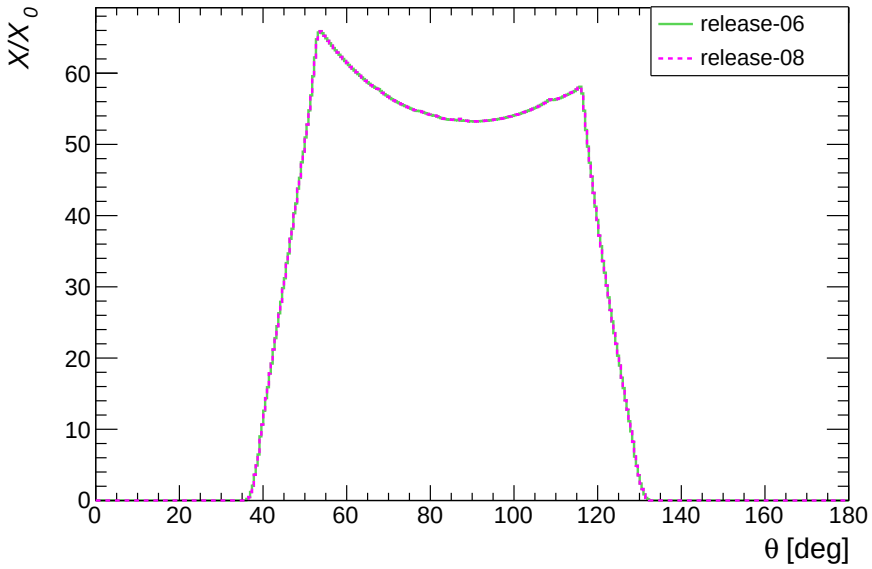

Figure 6.41 – Comparison of material in BKLM between release-06 and release-08. No changes are observed.

6.10 Outlook and Summary

The previous sections summarize the material content in all the detector components for Belle II. They also document the change that has occurred in the material model as a result of modifications to the geometry. While the geometry of the primary components of each detector has been implemented in the simulation, there remain tertiary components such as cables that haven't been modeled yet. These components are often outside the acceptance region, so don't impact the physics directly, or they are too complex to be modeled and are thus approximated in the simulation. A summary of the known deficiencies for each component is given below:

- SVD: Chapter 5 highlighted the implementation of the clamps in the ladders of the SVD. The current implementation approximates them as a

rectangular slab but in reality they are u-shaped and envelop the pipe. Future modifications should try to implement the shape more accurately.

- CDC: Cooling pipes and high/low voltage cables have not yet been implemented. While it is difficult to model cables individually, the plan is to implement some virtual material to account for their density in the material model in release-10 of basf2. Note that these parts are outside the acceptance so they won't impact the tracking.
- ARICH: There is a 1mm thick aluminum plate missing that closes the photo-detector box on its backside. In addition, there are cables, cooling pipes and some PCB boards missing.
- TOP: Pipes and cables have not yet been implemented.
- ECL: The missing parts are: cables, electronics and cooling pipes in the barrel and the backward region, small bolts, nuts and screws. All these parts are behind the crystals so they should not affect the energy resolution. In addition, compared to the stainless steel which the detector is made of, these parts contribute a very small portion to the material budget.

7

Conclusion

The goal of this thesis was to study the material content of the Belle II detector. Chapters 5 and 6 presented these studies in two different ways. Chapter 5 offered a detailed look into both measured and simulated material profiles for the vertex detectors. The discrepancies between the two profiles was highlighted and improvements were made to the simulation to reduce the disagreement between the two. In chapter 6, the material profile of each subsystem in the basf2 simulation was presented. In particular, emphasis was laid on studying the impact of the material changes to the simulation between two releases. The modifications made to the geometry that led to these changes were itemized and documented.

These studies serve as a first review of the material in the basf2 simulation. Since data is not available for Belle II yet, this is the only method of validating the material model. Once Belle II starts data taking, more detailed studies can be conducted which compare the photon conversion efficiency between data and Monte Carlo simulations. The rate of photon conversion is related to the material in the detector; these studies can thus yield information about how well the material is modeled in the simulation and will serve a second level of validation.

Bibliography

[1] T. Ferbel. *The Standard Model: Techniques and Concepts of High Energy Physics*. Kluwer Acad. Publ., 1999.

[2] D. Griffiths. *Introduction to Elementary Particles*. Wiley, 2008.

[3] P. Ramond. *Group Theory: A Physists Survey*. Cambridge, 2010.

[4] Wikipedia. *Standard Model*. Wikimedia Commons, 2017.

[5] S. L. Glashow *et al*. *Partial-symmetries of weak interactions*. Nuclear Physics, 22(4):579 - 588, 1961.

[6] G. F. Brand *et al*. *Atoms and Nuclei*. Sydney University Physics Education Reserach Group Notes, 1993.

[7] K. A. Olive *et al*. *Review of Particle Physics*. Chin. Phys., C38:090001, 2014.

[8] C. Grupen and B. A. Shwartz. *Particle Detectors*. Cambridge University Press, 2008.

[9] B. Golob *et al*. *Amount of material in the Belle-II simulation*. Belle2 Internal Note, 2015.

[10] J. Lettenbichler. *Real-time Pattern Recognition in the Central Tracking Detector of the Belle II Experiment*. Master's thesis, Technical University of Vienna, 2016.

[11] T. Abe *et al*. *Belle II Technical Design Report*. 2010.

[12] M. Prim. *Study of material effects in track fitting and improvement of the K_S^0 reconstruction at Belle II*. Master's thesis, KIT, 2015.

[13] M. Ritter. *Measurement of the branching fraction and time dependent CP asymmetry in $B^0 \to D^{*-} D^{*+} K_s^0$ decays at the Belle experiment*. PhD thesis, Munich U., 2013.

[14] C. Pulvermacher. *Analysis Software and Full Event Interpretation for the Belle II Experiment*. PhD thesis, KIT, Karlsruhe, 2015.

[15] A. Abashian *et al. The Belle detector*. Nuclear Instruments and Methods in Physics Research Section A: Accelerators, Spectrometers, Detectors and Associated Equipment, 479(1),117 - 232, 2002.

[16] L. Zani. *Measurement of the branching fraction of the baryonic decay mode $B^0(\bar{B}^0) \to p p \bar{p} \bar{p}$ at Babar and future prospects at Belle II*. Master's thesis, University of Pisa, 2015.

[17] PXD collaborators. *Flip-chip and SMD assembly of Belle-II PXD Pixel Sensors*. Internal Interface document, Max-Plank-Institute, 2013.

[18] H. Aihara *et al. Belle SVD2 vertex detector*. Nuclear Instruments and Methods in Physics Research Section A: Accelerators, Spectrometers, Detectors and Associated Equipment, 568(1):269 - 273, 2006.

[19] O. Frost. *A Local Tracking Algorithm for the Central Drift Chamber of Belle II*. Master's thesis, KIT, 2013.

[20] A. Fodor. *Design and Simulation of Beam-Background Monitors in the Vicinity of the Electromagnetic Calorimeter for the Belle II Experiment*. Master's thesis, McGill University, 2016.

[21] Z. Drasal. *Measurement of Time-Dependent CP Violation in $B^0 \to \eta_c K^0_S$ at Belle Experiment, Optimization Studies of the Belle II Vertex Detector*. PhD thesis, Charles U., 2013.

[22] A. Moll. *The software framework of the Belle II experiment*. J. Phys. Conf. Ser., 331:032024, 2011.

[23] U. Stolzenberg *et al*. *Radiation length imaging with high-resolution telescopes*. arXiv:1609.02402, 2016.

[24] U. Stolzenberg *et al*. *X_0 imaging of PXD and SVD sensors: Review of material budget estimations*. 10th VXD workshop in Santander, 2016.

[25] U. Stolzenberg *et al*. *Radiation length imaging with high-resolution telescopes*. Proceedings of Science for the 38th International Conference on High Energy Physics, 2016.

[26] H. A. Bethe. *Moliere's theory of multiple scattering*. Phys. Rev., 89:1256-1266, 1953.

[27] V. L. Highland. *Some practical remarks on multiple scattering*. Nuclear Instruments and Methods, 129(2):497 - 499, 1975.

[28] M. Uchida. *CDC Geometry from DB*. Technical report, Tokyo Tech, 2016.